

The New Generation Planetary Population Synthesis (NGPPS) VI. Introducing KOBE: Kepler Observes Bern Exoplanets [★]

Theoretical perspectives on the architecture of planetary systems: Peas in a pod

Lokesh Mishra^{1,2★★}, Yann Alibert¹, Adrien Leleu², Alexandre Emsenhuber^{1,3}, Christoph Mordasini¹, Remo Burn¹,
Stéphane Udry², and Willy Benz¹

¹ Institute of Physics, University of Bern, Gesellschaftsstrasse 6, 3012 Bern, Switzerland

² Geneva Observatory, University of Geneva, Chemin Pegasi 51b, 1290 Versoix, Switzerland

³ Lunar and Planetary Laboratory, University of Arizona, 1629 E. University Blvd., Tucson, AZ 85721, USA

Received 9 March 2021;

ABSTRACT

Context. Observations of exoplanets indicate the existence of several correlations in the architecture of planetary systems. Exoplanets within a system tend to be of similar size and mass, evenly spaced and often ordered in size and mass. Small planets are frequently packed in tight configurations, while large planets often have wider orbital spacing. Together, these correlations are called the peas in a pod trends in the architecture of planetary systems.

Aims. In this paper, these trends are investigated in theoretically simulated planetary systems and compared with observations. Whether these correlations emerge from astrophysical processes or the detection biases of the transit method is examined.

Methods. Using the Generation III Bern Model, synthetic planetary systems are simulated. KOBE, a new computer code, simulates the geometrical limitations of the transit method and applies the detection biases and completeness of the Kepler survey. This allows simulated planetary systems to be confronted with observations.

Results. The architecture of synthetic planetary systems, observed via KOBE, show the peas in a pod trends in good agreement with observations. These correlations are also present in the theoretical underlying population, from the Bern Model, indicating that these trends are probably of astrophysical origin.

Conclusions. Physical processes, involved in planet formation, are responsible for the emergence of evenly spaced planets with similar sizes and masses. The size/mass similarity trends are primordial and originate from the oligarchic growth of protoplanetary embryos and the uniform growth of planets at early times. Later stages in planet formation allows planets, within a system, to grow at different rates thereby decreasing these correlations. The spacing and packing correlations are absent at early times and arise from dynamical interactions.

Key words. Planetary systems – Planets and satellites: detection – Planets and satellites: formation – Planets and satellites: dynamical evolution and stability

1. Introduction

1.1. Motivation

Since the discovery of 51 Pegasi b, the first planet found to orbit another main-sequence star by Mayor & Queloz (1995), technological advancements have engendered the possibility to address the question: How common are Earth-like worlds in the habitable zone of Sun-like stars? Addressing this question NASA's space telescope – the *Kepler Mission* – measured the brightness of 198,709 stars for ~ 3.5 years with a fixed field-of-view pointing towards the Milky Way galactic plane (near the Cygnus-Lyra constellation) (Borucki 2016; Twicken et al. 2016). As a planet passes in front of a star, it can result in a measurable and periodic reduction in the flux coming from this star. Utilizing this method, the transit method, Kepler discovered and characterized thousands of exoplanets (Borucki & Summers 1984; Borucki et al. 2010; Borucki et al. 2011; Thompson et al. 2018). With

over 4,000 planetary candidates around over 3,000 stars¹, observations have revealed a staggering diversity in the nature of exoplanets (Armstrong et al. 2020; Hoeijmakers et al. 2018; Winn et al. 2018; Kreidberg et al. 2014; Sing et al. 2016; Santerne et al. 2019; Espinoza et al. 2020; Demory et al. 2016; Evans et al. 2016; Udry & Santos 2007). The rich diversity observed in exoplanets, fortuitously, also extends to the architecture of multi-planetary systems (Lissauer et al. 2011; Fabrycky et al. 2014; Winn & Fabrycky 2015).

The arrangement of multiple planets and the collective distribution of their physical properties around host star(s) characterizes the architecture of a planetary system. This implies that the architecture of any planetary system is an outcome of all the physical processes that lead the system to its present state. The architecture of a planetary system may reflect several simultaneous processes, such as: (a) specific formation pathway of individual planets, (b) secular and/or chaotic dynamical interactions, (c) configurations that are stable over billions of years, (d)

[★] KOBE is available at: <https://github.com/exomishra/kobe>.

^{★★} Correspondence: Lokesh Mishra (exomishra@gmail.com)

¹ Based on a September 2020 query of the Extrasolar Planets Encyclopaedia (Schneider et al. 2011).

initial conditions coming from the star and the protoplanetary disks, or (e) the astrophysical environment surrounding the star forming region. Specifically, the extent to which planet formation is stochastic remains unknown. Explaining the wide diversity observed in the system architecture remains an open problem (Winn & Fabrycky 2015). It is possible that planet formation is dominated by the same physical processes, but the large diversity in initial conditions leads to a wide variety of exoplanets and system architectures (Benz et al. (2014); Mordasini (2018)).

Amidst the observed diversity in the architecture of exoplanetary systems several trends have emerged (Ciardi et al. 2013). One example of such a trend is the so called ‘peas in a pod’ trend, which is the subject of this paper. Empirical trends in the system architecture serve two key purposes. Firstly, these trends provide hints about underlying physical processes. Thus, these trends posit additional constraints on theory. Secondly, as the understanding of exoplanetary astrophysics matures, reproduction of these trends in numerical calculations becomes a crucial testing ground amongst competing models. Perhaps, several of the observed correlations in planetary system architecture are unifiable, facilitating simpler physical explanations to emerge.

1.2. General Overview – Peas in a Pod

The California-Kepler Survey (CKS) improved the characteristics of 1,305 planet-hosting stars found by Kepler (Petigura et al. 2017) leading to an improvement in the characteristics of 2,025 planets transiting these stars (Johnson et al. 2017). Analysing 355 multi-planetary systems from the CKS dataset, hosting 909 planets, Weiss et al. (2018) (hereafter W18) reported several correlations in the properties of adjacent planets – akin to *peas in a pod*. They find that adjacent planets in a system tend to be similar in size, $R_{\text{outer}}/R_{\text{inner}} \approx 1^2$. This trend was already suggested by Lissauer et al. (2011) based on the first four months of Kepler’s observations. In addition, W18 report that $\sim 65\%$ of adjacent pairs in their dataset are size-ordered – the outer planet being larger than the inner planet. This trend was also hinted by Ciardi et al. (2013). For planetary systems with 3 or more planets, W18 find that the orbital spacing ($P_{\text{outer}}/P_{\text{inner}}$) of the first pair of planets is similar to the orbital spacing of the next pair of planets. They also report a correlation in the packing of planets within a system: smaller planets often have smaller orbital spacing, while large planets tend to have larger orbital spacing.

Using transit timing variations, Hadden & Lithwick (2017) inferred the masses and eccentricity of 145 planets hosted in 55 Kepler planetary systems. Studying this dataset, Millholland et al. (2017) show that planets, within a system, tend to have similar masses and are often ordered in mass; the outer planet being more massive than the inner planet. Additionally, Wang (2017) also reports similarity in mass in 29 systems detected by the radial-velocity method.

Pertaining to these trends, two kinds of studies have emerged. While some studies have explored theoretical aspects to better explain/quantify the observations (e.g. Mulders et al. 2020), other authors find little evidence for peas in a pod in their analysis (Murchikova & Tremaine 2020). For size-ordering, Kipping (2018) investigated whether traces of initial conditions of planet formation are removed by dynamical evolution. A tally score $T = \sum_{\text{pairs}} t_i$ is defined which tracks whether the radius of an outer adjacent planet is more ($t_i = +1$) or less ($t_i = -1$) than

its inner neighbour. The number of different ways for a planetary system to obtain the same tally score T , is interpreted as the entropy of the system.³ They find that Kepler systems have lower entropy than expected from randomly constructed systems, implying that initial conditions for Kepler systems and their formation pathways could be potentially inferred. Adams (2019) finds that energy optimization in planetary pairs, assuming fixed total angular momentum and total mass for a given orbital spacing, leads to planets in circular orbits with no mutual inclination and nearly equal masses. However, when the total mass in the planetary pair exceeds a threshold ($\sim 40 M_{\oplus}$ for $a \sim 0.1$ AU), energy optimization can cause one planet to gain most of the mass (Adams et al. 2020). Xu et al. (2018) suggest that ejection of small planets, caused by dynamical interactions, provides a possible explanation for the observed correlations. MacDonald et al. (2020) find that in-situ formation of $1 - 4 R_{\oplus}$ sized planets while varying the amount of solids present in the inner region of the proto-planetary disk, can lead to systems with similar sized planets with correlated orbital spacings.

Although highly successful in discovering exoplanets, the transit method suffers from inherent geometric limitations (only planets whose orbits are, serendipitously, edge-on can transit) and detection biases (large planets close to a small quiet star are strongly favoured). This strongly limits our knowledge of the underlying ‘ground-truth’ distribution of exoplanets (Borucki & Summers 1984; Barnes 2007; Kipping & Sandford 2016)⁴. Nevertheless, since these effects are well-understood, observations are de-biased to understand the true exoplanetary population. Claiming that the peas in a pod trend is not astrophysical, Zhu (2020) suggests that the observed correlations are due to detection biases (debated further in Weiss & Petigura (2020)). However, using a parametrized model of planetary systems, He et al. (2019) find that clusters of similarly sized and spaced planets provide better fit to Kepler observations.

1.3. This work – How theory meets observations

Planet formation begins in protoplanetary disks around young pre-main sequence stars. The physical environment in and around these disks sets the initial condition for planet formation. The theory of planet formation and evolution describes the physical processes which links these initial conditions to the resultant planets. In Sect. 2, the planet formation model used in this work, the Generation III *Bern Model* is described. Next, in order to compare theory with observations at the population level, theoretical planetary populations are required⁵. In Sect. 3, the *New Generation Planetary Population Synthesis* (NGPPS) used in this work is presented.

Since nature’s underlying exoplanetary population is only partially accessible via the transit method, observations cannot be compared directly with the output of population synthesis. To facilitate this comparison, the detection biases of an observational survey must be placed on the synthetic populations. In this work, the detection biases of the Kepler survey are applied on the output of NGPPS by simulating relevant parts of the Kepler pipeline and Kepler’s Robovetter (Twicken

² Note: lowercase r is used for radial distance of an object (e.g. distance from the star), while capital R is used to denote the radius of an object.

³ Alternative definitions of entropy are also explored by incorporating a memory-like term to include size-ordering from one adjacent pair of planets to the next adjacent pair of planets.

⁴ For example, Sandford et al. (2019) estimate around $\approx 2,400$ more exoplanets reside in 1537 planet hosting FGK stars observed by Kepler.

⁵ A set of hundreds or thousands of individual planetary systems are, here, referred to as a population.

et al. 2016, 2018; Thompson et al. 2018). Section 4 introduces a new computer code, KOBE (Kepler Observes Bern Exoplanets), which mimics the Kepler transit survey for synthetic planetary systems. KOBE computes a populations of synthetic planets which are on the same footing as Kepler’s planetary candidates. The theory can now be confronted with Kepler’s findings, as is done in this and forthcoming papers.

KOBE-multi-planetary systems are introduced and compared with the observations in Sect. 5. In Sect. 6, the peas in a pod trends are formally stated and the architecture of synthetic systems is examined. In Sect. 7, the role of adding detection biases is elucidated. Theoretical scenarios that lead to the peas in a pod trends are discussed in Sect. 8. Section 9 concludes this paper by summarizing the main results and discussing possible explorations in future works. Appendix A explains the correlation between average size of planets and their mutual separation.

The aim of this paper is three-fold: investigate the peas in a pod trends in the architecture of theoretical planetary systems and compare with observations, understand the role of geometrical limitations and detection biases on the observed trends, and explore physical mechanisms which could explain the peas in a pod correlations.

2. Generation III Bern Model

The *Bern Model* is a global model of planet formation and evolution based on the core-accretion paradigm (see Pollack et al. 1996; Alibert et al. 2004, 2005)⁶⁷. From its initial inception in Alibert et al. (2005), the model has undergone several updates (Mordasini et al. 2008, 2009; Alibert et al. 2011; Mordasini et al. 2012c,b,a; Alibert et al. 2013; Fortier et al. 2013; Marboeuf et al. 2014; Thiabaud et al. 2014; Dittkrist et al. 2014; Mordasini et al. 2015, 2017). The generation III *Bern Model*, used in this work, is presented in detail in Emsenhuber et al. (2020a,b) (hereafter Paper I and Paper II respectively) (for reviews, see Benz et al. 2014; Mordasini 2018). For completeness, a summary of the major physical processes included in the model is given below. Figure 1 shows a schematic diagram of the key physical processes included in the model.

2.1. Before planet formation begins

The gravitational collapse of cold, diffuse molecular clouds leads to the formation of (multiple-) stars and circumstellar disks. Conservation of angular momentum implies that gravitationally bound material will flatten into a protoplanetary disk. Dust and gas, from the cloud, falls onto the protostar and its disk for about 10^5 yr (Nakamoto & Nakagawa 1994; Baillié et al. 2019). The surrounding envelope is cleared by this time – either due to star/disk accretion or dispersion via jets and outflows – and the thermal emission from this system resembles that of a classical T-Tauri Star (Tychoniec et al. 2018). Although debated, dust grains (10^{-6} m) grow quickly by sticky collisions, or gravitational instabilities into kilometre-sized planetesimals (Youdin 2008; Johansen et al. 2007; Williams & Cieza 2011). A swarm of planetesimals, interacting gravitationally, undergo rapid runaway growth wherein larger planetesimals grows faster (Kokubo

& Ida 1998). When runaway growth is no longer possible, either due to significant velocity disruptions or lack of material to accrete, oligarchic growth begins. The resulting lunar mass bodies, called protoplanetary embryos, emerge rapidly $\sim 10^4$ yr (Kokubo & Ida 2002). This stage marks the starting point for the Bern Model and is sketched in panel (c) of Fig. 1.

The model studies the subsequent growth of protoplanetary embryos, which are embedded in a disk of planetesimals and gas. Multiple physical processes, interactions and phenomenon are simultaneously occurring in this star-disk-embryo system, resulting in many kinds of planets and system architectures. The implementation of stellar and protoplanetary disk evolution is presented in Appendix B.1.

2.2. Planet Formation

In core-accretion models, planet formation occurs in two major steps. Initially all embryos grow by accreting planetesimals at a rate of $\sim 10^{-5} M_{\oplus}/\text{yr}$, while the rate of gas accretion is very small (Alibert et al. 2005; Pollack et al. 1996). Eventually, the protoplanetary gas becomes gravitationally bound to these growing planetary cores. If the mass of a core crosses a certain critical mass threshold ($\sim 10 M_{\oplus}$) while the nebular gas is still present, it can undergo runaway gas accretion becoming a giant planet (in a few Myrs). In contrast, planetary cores failing to cross the mass threshold, do not undergo runaway gas accretion. Accreting solids from their feeding zones, these cores undergo collisions with other cores resulting in a diverse range of planets (≈ 10 -100 Myrs) (see panel (d) of Fig. 1). The implementation of solid and gaseous accretion is described in Appendix B.2.

2.3. Additional Physics

The Bern Model considers several additional physical mechanisms as shown in panel (e) of Fig. 1.

Orbital Migration: Gravitational interactions between the planet and the disk lead to orbital migration of planets and the damping of eccentricity and inclination. The exchange of angular momentum, via torques, usually results in an inward migration of planets. Low mass planets undergo Type I migration, which is implemented following the approach of Coleman & Nelson (2014); Paardekooper et al. (2011). Massive planets can open a gap in the gas disk and undergo Type II migration, which is implemented following Dittkrist et al. (2014). In type II migration, some planets can migrate outwards. Planets inside the gap, if detached, continue to accrete until the disk disappears (Kley & Dirksen 2006).

N-body interactions: Gravitational interactions between the star and multiple planets are included through the *N*-body code mercury (Chambers 1999). This formation stage tracks the dynamical evolution of planetary orbits, resonances, and collisional growth of planets (Alibert et al. 2013). Orbital migration and damping are coherently included in the *N*-body. The *N*-body computations are performed for 20 million years since the start of the model.

After N-body: The model calculates the internal structure of all planets for 10 billion years, after which calculations are stopped. This stage includes effects like atmospheric escape (Jin et al. 2014), bloating (Sarkis et al. 2021) and tidal migration.

⁶ Readers who are well-versed with the Bern Model and its updates may skip to Sect. 4, where KOBE is introduced. Other readers may use this introductory section as a starting point for key concepts and relevant literature for planet formation in general, and Bern Model in particular.

⁷ A global model, which comprises of theoretical models of individual physical processes linked together coherently, calculates the final planetary system based on a set of initial conditions.

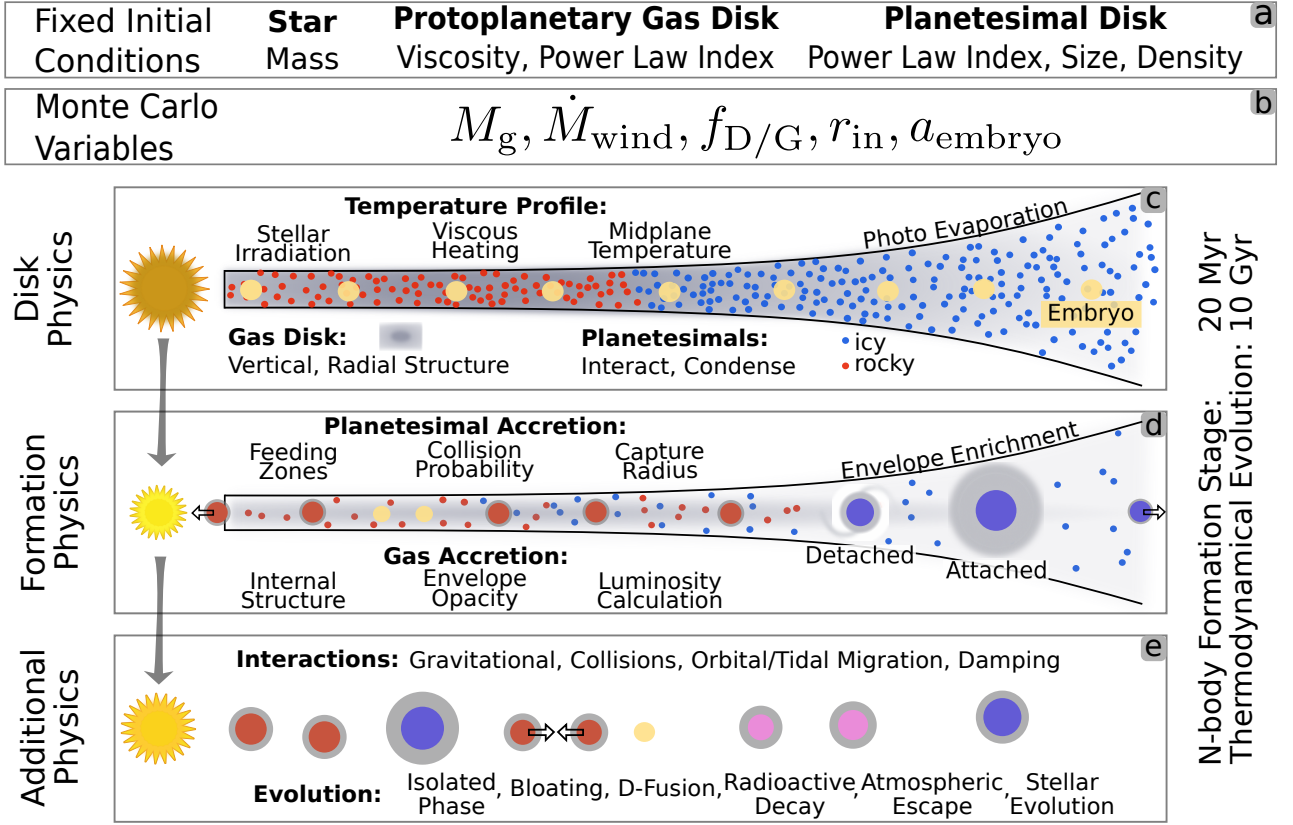


Fig. 1. The Bern Model: A schematic diagram illustrating the breadth of physical processes incorporated in the Generation III Bern Model of Planet Formation and Evolution. Panels (a) and (b) show the fixed and varying initial conditions, respectively. Physical processes that are relevant to the protoplanetary disk are indicated in panel (c). It represents a snapshot of the starting point of the model: several protoplanetary embryos are embedded in a disk of gas and planetesimals. The processes which govern planet formation and evolution are displayed in panel (d). In panel (e), additional physics incorporated in the model is shown. The arrows indicate the evolution of a fixed mass star. Most of the depicted physical processes occur simultaneously and not all processes are shown. See text for summary and [Paper I](#) for details. Figure is not drawn to scale.

2.4. What is meant by the radius of a planet?

In the Bern Model, all planets have a spherically symmetric structure composed of several layers of accreted material. These layers are: iron core, silicate (perovskite MgSiO_3) mantle, and water ice (if accreted) for the planetary core, and a H/He gaseous envelope (if accreted). For planets without any gaseous envelope the radius is obtained by solving the core internal structure (see [Paper I](#)). In this study, core radius and radius is used interchangeably for such planets.

Planets with gaseous envelopes, however, do not offer a well-defined surface. The radius of such planets depends on the wavelength at which transits are measured ([Heng 2019](#)). To facilitate comparison with transit observations, in this work the concept of transit radius is used. Transit radius is the radial distance from the centre of a planet where the optical depth for a visible ray of light grazing the planet's terminator (chord optical depth) is $2/3$ ([Burrows et al. 2007](#); [Guillot 2010](#)). In this study, transit radius and radius will be used interchangeably for such planets.

3. New Generation Planetary Population Synthesis

Population synthesis provides a way to compare theory with observations of exoplanets and their architecture at the population level ([Ida & Lin 2004](#); [Mordasini et al. 2009](#)). The framework of population synthesis rests on one key assumption – the rich diversity in nature's exoplanetary population emerges due to a variety of possible initial conditions and N -body interactions

([Benz et al. 2014](#); [Mordasini 2018](#)). Thus, multiple runs of a global model (while varying initial conditions for disk and star, and including N -body interactions) can produce theoretical exoplanetary populations possessing some of the observed diversity. Panels (a) and (b) of [Fig. 1](#) show the fixed and varying initial conditions.

The New Generation Planetary Population Synthesis (NGPPS) consists of synthetic planetary systems computed from the generation III Bern Model (see [Paper II](#)). The Bern Model simulates planet formation and evolution by following the simultaneous growth of multiple planetary embryos embedded in a protoplanetary disk. However, since the number of embryos in a disk is unknown, it is treated as a free parameter. In this work, three nominal models are studied with 20, 50 and 100 embryos. Each model is used to simulate 1 000 planetary systems, wherein different initial conditions are assigned to each system in a Monte Carlo manner. The Monte Carlo variables are: (for details see [Paper II](#))

1. Initial mass – Protoplanetary gas disk, M_g :

The initial distribution of gas disk mass, M_g , follows the mass distribution of Class I disks reported by [Tychoniec et al. \(2018\)](#). The values range from $0.004 M_\odot$ to $0.16 M_\odot$. This governs the initial spatial distribution and surface density profile of the disk via eq. [B.3](#).

2. Disk lifetime – Photoevaporation Rate, \dot{M}_{wind} :

Varying \dot{M}_{wind} allows the model to have disks with different lifetimes. Disk lifetimes closely follow the observed disk lifetimes (see details in Paper II).

3. Stellar metallicity – Dust to Gas ratio, $f_{\text{D/G}}$:
The initial mass of the solids in the disk is a fraction of the initial mass of the gas disk M_g , (the dust to gas ratio $f_{\text{D/G}}$). Varying this ratio allows the model to capture the observed variation in stellar metallicities. This assumes the following relation,

$$10^{[\text{Fe}/\text{H}]} = \frac{f_{\text{D/G}}}{f_{\text{D/G},\odot}}, f_{\text{D/G},\odot} = 0.0149 \text{ (Lodders 2003)}. \quad (1)$$

The distribution of metallicities is in the range -0.6 to 0.5 and follows that of Santos et al. (2005). Additionally, it is assumed that all of the dust in the solid disk is converted to planetesimals⁸.

4. Inner edge of disk, r_{in} :
Regions of the disk which are close to the star interact with the stellar magnetic field resulting in stellar accretion, ejection, outflows, etc. The inner edge of the disk is taken at the co-rotation distance from the star, i.e. the distance where the Keplerian orbital period matches the rotation period of the star. The stellar rotation periods are sampled from observations (Venuti et al. 2017). The distribution has a mean value of 4.7 d (corresponding to 0.055 au), while the lower end is truncated at 0.77 d.
5. Initial location of planetary embryo, a_{embryo} :
Planetary embryos are initialized with a mass of $10^{-2} M_{\oplus}$. The initial location of embryos follows a distribution which has a uniform probability in the logarithm of distance between r_{in} and 40 au. It is ensured that all embryos are at least $10 R_{\text{H}}$ apart from each other, resulting from their run-away growth (Kokubo & Ida 1998, 2002).

The characteristics of all NGPPS planetary systems are strongly distorted by failed embryos due to their tremendous numbers. As a working definition, planetary embryos which fail to grow more than 10 times from their initial masses are considered failed embryos. To simplify the discussion that follows, failed embryos are removed from the underlying population by removing objects with mass below $0.1 M_{\oplus}$ ⁹. In addition, for simplicity, only the results of the 100 embryo population are presented (except Sect. 8.2 where the 20 and 50 embryo populations are also discussed).

4. Kepler Observes Bern Exoplanets (KOBE)

Kepler Observes Bern Exoplanets (KOBE) is a new computer code which simulates transit survey of exoplanets¹⁰. Suppose a population of synthetic planets (as in Bern Model’s NGPPS) is hypothetically observed by Kepler’s transit survey. The aim of KOBE, in this scenario, is to identify those synthetic planets which would have been detected by the Kepler pipeline.

Calculations in KOBE are organized in three sequential modules. KOBE-Shadows, the first module, is tasked with finding

transiting planets from a synthetic population of planets. This module produces the KOBE-Shadows catalogue which consists of systems with at least one transiting planet. Although, all of the planets in this catalogue will transit, but not all of them will be detected. The next module, KOBE-Transits, computes transit related parameters for transiting planets. Planets which produce a strong transit signal-to-noise ratio (SNR) are detected. Planets which transit at-least 2 times and have $\text{SNR} \geq 7.1$ constitute the KOBE-periodic threshold crossing event ($p\text{TCE}$) catalogue¹¹. The last module, KOBE-Vetter, applies the completeness and reliability of Kepler pipeline by emulating Kepler’s Robovetter (Twicken et al. 2016, 2018; Thompson et al. 2018). Transiting planets that are dispositioned as planetary candidates, by KOBE-Vetter, make up the KOBE catalogue. The synthetic population in this catalogue is comparable to the exoplanet population discovered by Kepler. Later sections of this paper, analyse the architecture of planetary systems in the KOBE catalogue and compare it to observations. In a forthcoming paper, the KOBE catalogue will be compared with other findings of Kepler.

These three modules encapsulate the three different kinds of biases and limitations of a transit survey. KOBE-Shadows accounts for the geometrical limitation of the transit method. A planet can only transit when its orbits is aligned with respect to an observer. KOBE-Transits applies the detection biases coming from physical limitations: Large planets, in tight orbits, around a quiet star are strongly favoured. Finally, KOBE-Vetter imprints the completeness and reliability of a transit survey. In Appendix C, the three modules are described in detail.

4.1. Effect of KOBE on the 100 embryo population

To understand KOBE’s effect, Fig. 2 presents the 100 embryo underlying population (in red) as it goes through each stage of calculation in KOBE. The figure shows normalized cumulative distribution for planetary radius (left) and period (right). The KOBE-Shadows catalogue is in orange, the $p\text{TCE}$ catalogue from KOBE-Transits is in light blue and the planetary candidates catalogue from KOBE-Vetter is in blue.

The shadow catalogue is dominated by planets which have high transit probability (eq. C.6), which is decided mostly by the star-planet distance and to a minor extent by the planet’s size. Therefore, the shadow catalogue closely follows the underlying population in radius, but not in period. The excess of planets in the shadow catalogue around $3 R_{\oplus}$ comes from a cluster of planets, in the underlying population, with high transit probability due to their low periods, $P < 10$ d. As shown in the period distribution, planets with $P < 10$ d make up 70% of the shadow catalogue, while they account for only 10% of the underlying population.

The $p\text{TCE}$ catalogue strongly favours large planets at shorter orbital distances. Therefore, in the radius distribution the tail of small sized planets in the $p\text{TCE}$ catalogue is shifted to right. About 30% of the planets in the shadow catalogue have $R_{\text{planet}} < 1 R_{\oplus}$, whereas only 10% of the $p\text{TCE}$ planets have $R_{\text{planet}} < 1 R_{\oplus}$. Requiring a minimum of 2 transits, implies that the maximum period of a planet in the $p\text{TCE}$ catalogue will be $P_{\text{max}} = (3.5 \times 365.25)/2 \approx 640$ d. This explains the sharp drop at 640 d in the period distribution of the $p\text{TCE}$ catalogue. The KOBE-Vetter catalogue closely resembles the $p\text{TCE}$ catalogue. Differences arise when the completeness, as emulated by KOBE-Vetter, is considerably low. As seen in Fig. C.2, this occurs for planets with large radii or large periods.

¹¹ Following W18, the minimum number of transits is fixed at 2.

⁸ In an alternative approach, some of the solid disk mass could be partitioned into pebbles. For a comparison of planet formation via pebble accretion and planetesimal accretion see Brügger et al. (2018, 2020).

⁹ Due to their small size, these objects are virtually undetectable via transit method and do not affect the results of this paper.

¹⁰ The current version of KOBE is designed to simulate NASA’s *Kepler* space telescope. However, KOBE is not limited to the Kepler survey and can be easily tweaked to simulate other transit surveys like TESS, PLATO (Ricker et al. 2014; Rauer et al. 2014).

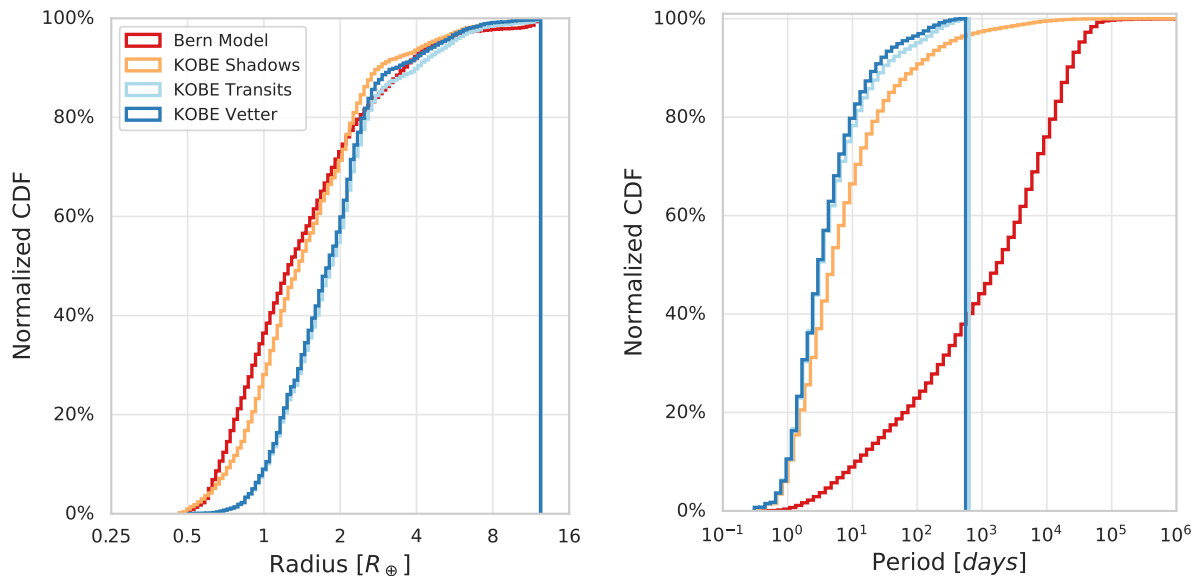


Fig. 2. This figure shows how a planetary population is affected as it goes through the various modules of KOBE. It shows the normalized cumulative distributions for radius (left) and period (right) for the 100 embryo population. The solid red curve represents the underlying population as calculated by the Bern Model. The orange curve is the output of KOBE-Shadows. KOBE-Transits’s p TCE catalogue is shown in light-blue, and the catalogue of planetary candidates, as vetted by KOBE-Vetter is shown in blue.

5. KMPS: KOBE Multi-Planetary Systems

In W18, selection cuts were placed to obtain a ‘high-purity’ population of planetary systems, the CKS-Multis (CKSM). The KOBE catalogue produced in the last section undergoes similar cuts. Planets with high impact parameter, $b > 0.9$, are removed. Planets with multi-transit SNR < 10 are also removed. Finally, planetary systems with only one remaining planet are removed. This creates a catalogue of KOBE’s multi-planetary systems, which are on the same footing as the CKSM catalogue coming from observations¹². Figures 3 and 4 present a comparison of the theoretically observed planetary population (KOBE in blue) with observations (CKSM in green) of exoplanets. Overall, the two catalogues have remarkable similarities and understandable differences. The underlying population (Bern Model in grey) is also shown.

The scatter plot in Fig. 3 (top) shows the radius of a planet as a function of its orbital period. It shows that the KOBE and CKSM planetary populations cover similar parameter space. A comparison with the grey points gives an impression of the planets that are missed by the transit method or removed by the selection cuts. In terms of period, the KOBE catalogue is bound by a vertical dashed line. This line marks the maximum period of a planet which can be found by KOBE. This comes from the requirement of at-least 2 transits (n_{tra} is fixed as t_{kepler}/P). There are two planets in the CKSM catalogue which have periods larger than KOBE’s maximum detectable period (KOIs: K00435.02 and K00490.02). For a given period, the dotted line approximates the minimum size of a planet which will produce a transit SNR of 10, around a $1 R_{\odot}$ star. There are some CKSM planets below this dotted line. These planets are orbiting a star of $R_{\star} < 1 R_{\odot}$.

5.1. Radius and Period distributions

Figure 3 also shows the normalized radius (top) and period (bottom) distribution of the KOBE, CKSM and Bern Model populations. For radius, the KOBE and CKSM populations are quite similar. The KOBE radius distribution shows the cumulative effects of both KOBE and the selection cuts placed on the underlying population. This distribution shows a bimodal nature with the two modes being around $1.4 - 1.7 R_{\oplus}$ and $2 - 3 R_{\oplus}$. The observed CKSM radius distribution also shows this feature. This is the well known radius gap seen around $2 R_{\oplus}$ (Fulton et al. 2017; Venturini et al. 2020). The CKSM population has relatively more planets with sizes between $3 - 4 R_{\oplus}$ than the KOBE population. This can be attributed to a dearth of $3 - 4 R_{\oplus}$ sized planets with $P < 100$ d in the underlying population. This is also reflected in the sharp drop seen in the period distribution of KOBE planets with $P \approx 100$ d. The radius distribution of the underlying population, however, does not show any radius gap. This is because the underlying population is dominated by small-sized planets which are at a large distance from the host-star. It is the cumulative effect of applying transit-probability (via KOBE-Shadows) and the detection biases of the transit method (via KOBE-Transits and KOBE-Vetter), which removes these small and distant planets. This allows the radius-valley in the theoretical population to be clearly seen.

The period distributions of the KOBE and the CKSM populations have similar slopes after their respective peaks. This is a reflection of the role played by transit probability (which decreases as $P^{-3/2}$). In the KOBE population, the period distribution peaks at about 3 d, while the CKSM distribution peaks around 5 d.

5.2. Multiplicity Distribution

The geometrical limitations of the transit method severely impacts the observed multiplicity of planets in a system. Multiplicity, for an observer, results from the overlap of transit shadow

¹² For simplicity, the KOBE multi-planetary system population will now be referred to as the KOBE population.

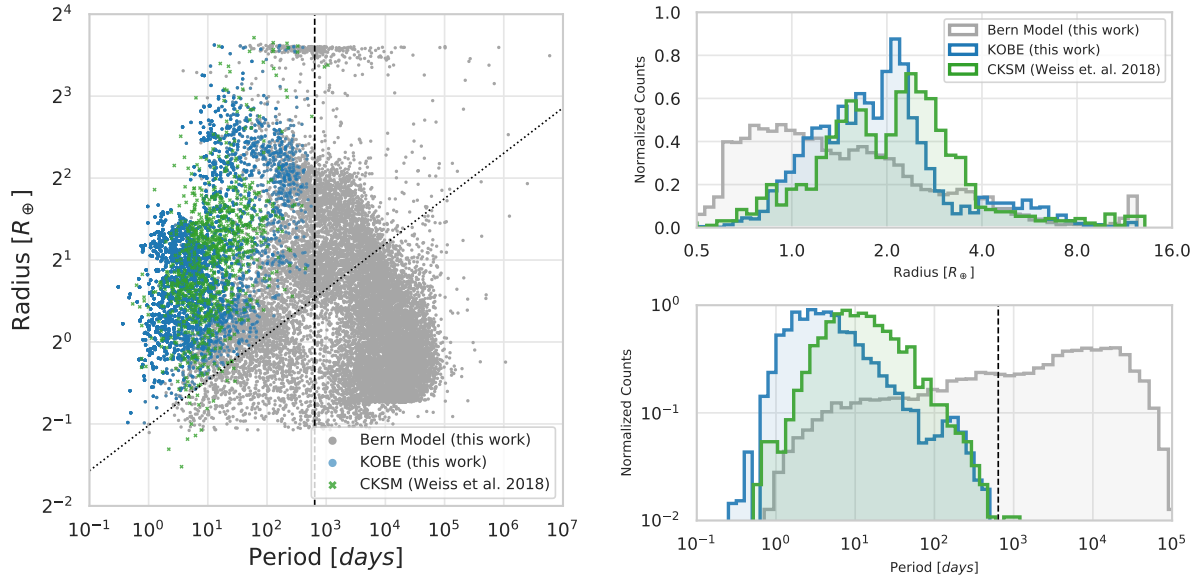


Fig. 3. Comparison of planetary populations: theoretical (blue) represents planets in multi-planetary systems found by KOBE and observations (green) are the CKS’s multi-planetary systems (CKSM). Left: A scatter plot with planetary radius on y-axis and period on x-axis. The dashed line shows the maximum period of a planet which can be found by KOBE. The dotted line shows the minimum radius of a planet around a $1 R_{\odot}$ star for producing a transit SNR of 10. The underlying theoretical population is shown in grey. Right: Comparison of radius (top) and period (bottom) distributions. The radius valley can be clearly seen in the planets found by KOBE and the California-Kepler survey.

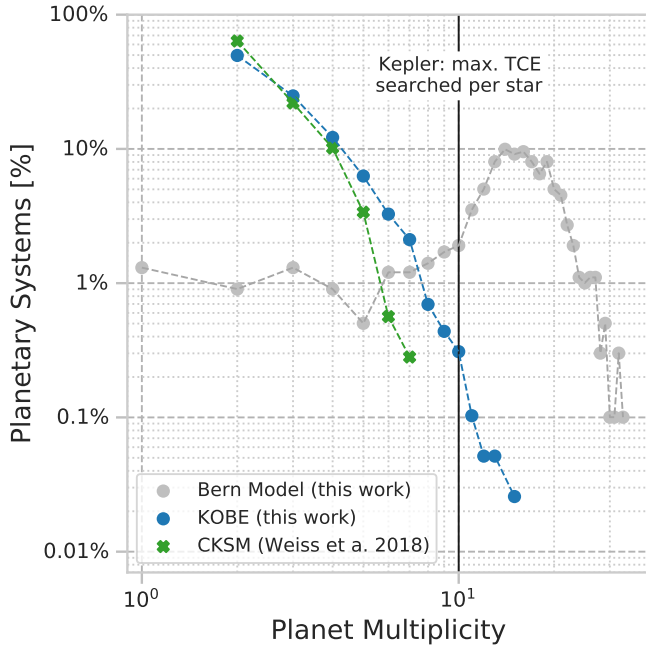


Fig. 4. Distribution of planetary multiplicity: Bern Model in grey, KOBE in blue, and observed CKSM in green. The solid black line marks the maximum number of TCE searches for a star performed by the Kepler pipeline.

band of multiple planets at the observer’s location (see Fig. C.1). Low mutual inclination between multiple planets leads to a large overlap in the transit shadow bands. This results in a higher probability for observers to find multiple transiting planets. The mutual inclination of planets is governed, in part, by the dynamical history of the system. Fig. 4 shows the multiplicity distribution.

The theoretical KOBE population shows a noteworthy similarity with the observed CKSM population. The vertical solid black line indicates the maximum number of TCEs, per star, which was searched by the Kepler pipeline (Twicken et al. 2016). The multiplicity distribution of both the KOBE and CKSM populations shows large differences from the underlying synthetic population. This is directly attributed to the geometrical limitations inherent in the transit method.

About 60% of systems in the CKSM catalogue have only 2 planets. The percentage of systems with higher multiplicity drops sharply, with less than 1% of CKSM systems having 6 or 7 planets. The KOBE catalogue closely follows the CKSM catalogue in the multiplicity distribution. KOBE systems with 2 planets are less frequent than CKSM (about 50%). However, for 3 or more planets the KOBE catalogue has more systems than the CKSM catalogue. This may arise due to the low mutual inclination between the planets formed in the Bern Model (Mulders et al. 2019).

6. Peas in a Pod

The so called ‘Peas in a pod’ trends in the architecture of planetary systems refer to correlations observed in the properties of adjacent exoplanets. The following collection of statements define the peas in a pod trends in the architecture of multi-planetary systems.

1. **Size:** Planets within a system tend to be either similar or ordered in size. Here, similarity implies that for two adjacent planets, $R_{\text{outer}}/R_{\text{inner}} \approx 1$. Two adjacent planets are said to be ordered in size, when the outer planet is larger than the inner planet, $R_{\text{outer}}/R_{\text{inner}} > 1$.
2. **Mass:** Planets within a system tend to be either similar or ordered in mass. Here, similarity and ordering are defined using a planet’s mass.
3. **Spacing:** For systems with 3 or more planets, the spacing between a pair of adjacent planets is similar to the spacing

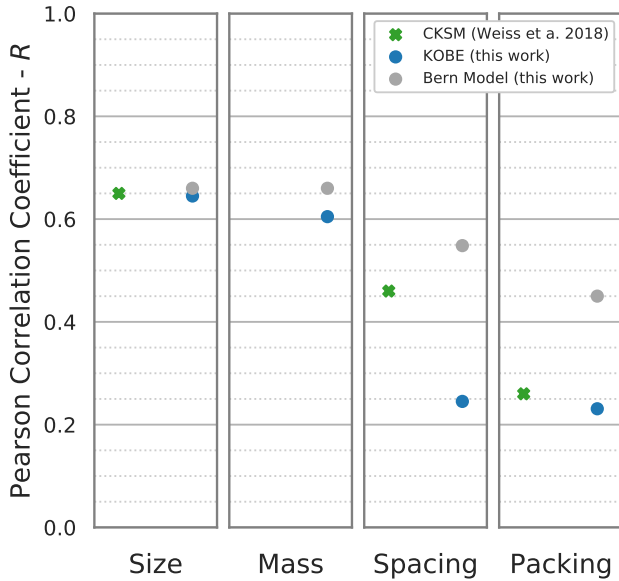


Fig. 5. Peas in a pod: a comparison of the correlations present in the theoretically observed KOBE catalogue (theory) and the CKSM catalogue (observations). Also shown are the correlations present in the underlying Bern Model population (grey).

between the next pair of adjacent planets. This is quantified by the ratio of period ratios for adjacent pairs of planets, $(P_{j+2}/P_{j+1})/(P_{j+1}/P_j) \approx 1$. The index j identifies different planets with $j = 1$ being the innermost planet and so on.

4. **Packing:** Small planets are found to be closely packed together, while large planets tend to have large orbital spacing. This is quantified by comparing the average radii of adjacent planets $(R_{\text{inner}} + R_{\text{outer}})/2$, with their period ratio $P_{\text{outer}}/P_{\text{inner}}$.

These statements take the results from W18 and Millholland et al. (2017) into account. These trends were examined in W18 by measuring the strength of correlations using Pearson-R correlation test. In this paper, the synthetic planets in the KOBE population are tested for the same correlations using the same correlation test. Figure 5 presents a comparison of the correlation coefficient found in the observed exoplanetary systems (CKSM) and the observable synthetic population (KOBE). There is a remarkable agreement in the correlations of size and packing. Although present in KOBE, the spacing correlations is not as strong as those found in CKSM. As transit observations do not yield planetary masses, the correlation coefficient for mass is not available for the CKSM systems. Each panel in Fig. 5 is discussed below with additional details. In Sect. 7 the role of detection biases in producing these correlations is examined ¹³.

6.1. Peas in a Pod: Radius

Following W18, before testing for correlations in size (and also in mass), all adjacent pairs of planets in the KOBE population are

required to undergo a swapping test. If both planets in a pair produce transit $\text{SNR} \geq 10$ when their orbital positions are swapped, then this pair is included for testing correlations. Figure 6 shows the radius of an outer planet as a function of the inner planet's radius, for the underlying (left) and the KOBE (right) populations. The middle panel shows the same for planets from the underlying population that could have been detected by KOBE ($P < 640$ d).

For the KOBE population, there is a strong (Pearson $R = 0.64$) and significant correlation present in the size of adjacent planets¹⁴. The size correlation between adjacent planets is also seen through the Spearman-R test (Spearman $R = 0.69$). This implies that adjacent planets in KOBE catalogue have sizes which are similar to their neighbours. The plot also shows that for 65% of adjacent pairs the outer planet is also the larger planet. This frequency of ordered adjacent pairs in KOBE is exactly the same as seen in CKSM (W18) and similar to the findings of Ciardi et al. (2013). This implies that the outer planet, in an adjacent pair of planets, is often the larger planet in the KOBE catalogue.

It is interesting to compare the size correlations present in the KOBE populations, with the size correlations present in the underlying populations. The underlying population (Fig. 6 (left)) shows strong (Pearson $R = 0.66$, Spearman $R = 0.64$) and significant ($p\text{-value} \ll 10^{-10}$) correlation in size of adjacent planets. This is an important result and it strongly suggests that size correlation between adjacent pairs of planets is already present in the underlying population. However, only 48% of pairs in the underlying population are ordered. Thus, there is an almost even chance for either the smaller or larger planet, in an adjacent pair, to be further out.

Keeping only detectable planets (with $P < 640$ d), shows the size-correlation present in the underlying population of detectable planets. Compared to the entire underlying population, this population shows a stronger size similarity and size ordering. Removing non-detectable planets tends to remove many small planets that occur frequently in the outer parts of a system. However, adjacent pairs where the outer planet is smaller are removed more often than the adjacent pairs where the outer planet is larger. This shows that the inner region of many planetary systems is populated by size-ordered pairs. This also explains the increase in size correlation, seen in this population, which arises from a decrease in adjacent pairs where the outer planet is larger.

The role of detection biases becomes clear when the KOBE population is compared with the population of detectable planets. Since, small planets are harder to detect via the transit method, many planets with $R_{\text{planet}} < 1R_{\oplus}$ are not found by KOBE. This effectively decreases the size similarity correlation. However, as the KOBE population is a subset of the population of detectable planets, it inherits the frequency of size-ordered pairs.

Overall, the theoretically observed KOBE catalogue shows similarity and ordering in the size of adjacent planets. These trends are in excellent agreement with observations. The theoretical underlying population of detectable planets also shows these correlations. While the size similarity and size ordering are affected by the detection biases – these correlations do not originate from detection biases of the transit method. This suggests that the correlations, seen in observations, may have an astrophysical origin.

¹³ In addition to the Pearson-R correlation test, the Spearman-R correlation test was also performed for all correlations. The Spearman-R tests for correlations (specifically monotonicity) in the rank of members of two datasets instead of their actual value.

¹⁴ Following W18, the size correlation coefficient Pearson R is calculated on the log of radius. Since the Spearman R is calculated on the rank of the members in a dataset, taking a log produces no difference on the coefficient's value.

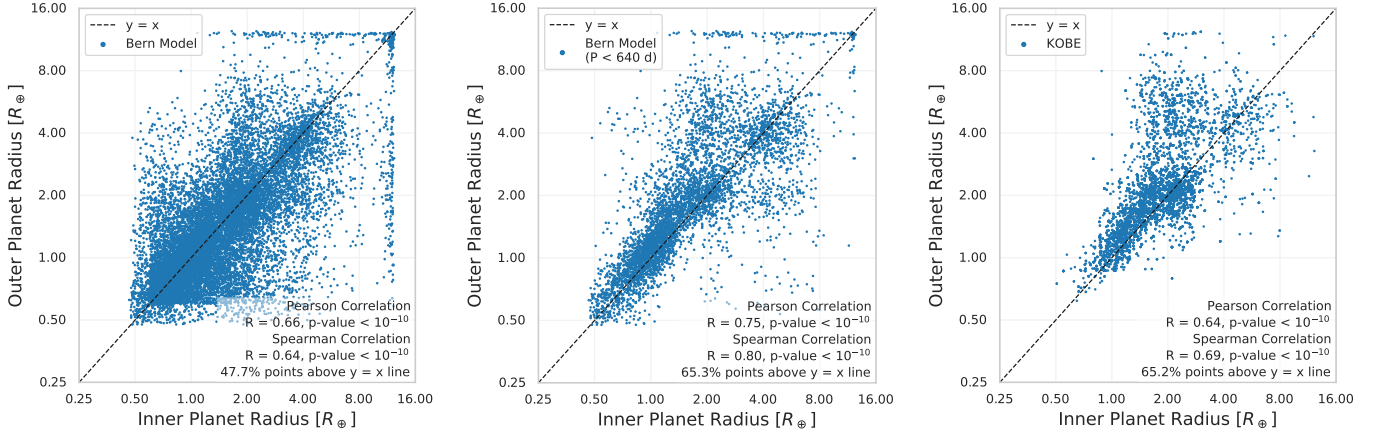


Fig. 6. Peas in a pod - Size: The sizes of adjacent planets are shown for the underlying population (left), underlying population of detectable planets ($P < 640$ d) (middle), and the theoretical observed planets (right). All populations show strong and significant correlation between the size of neighbouring planets. This suggests that planets tend to have sizes which are similar to their adjacent neighbours.

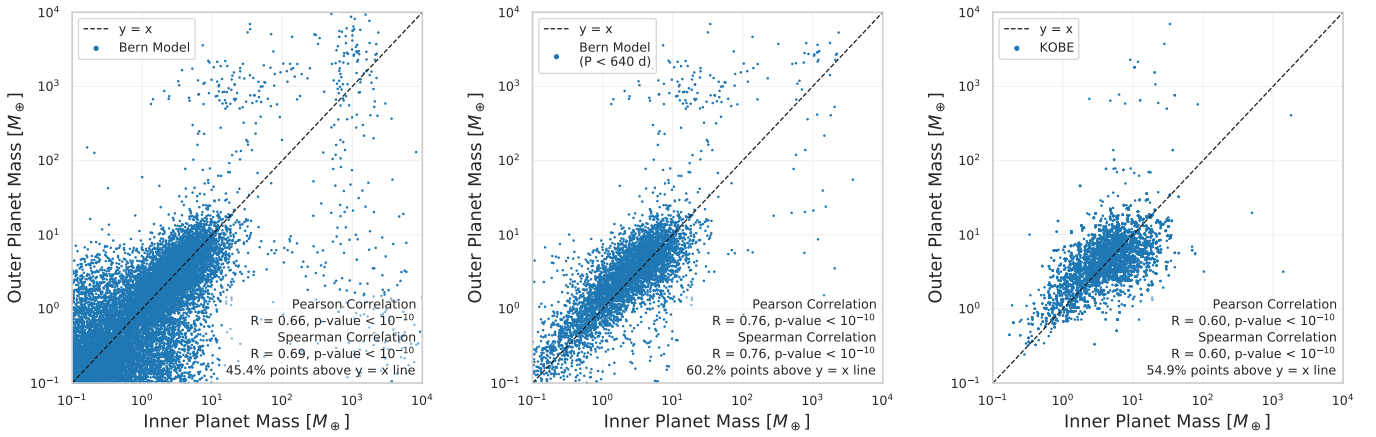


Fig. 7. Peas in a pod - Mass: The masses of adjacent planets are shown for the underlying population (left), underlying population of detectable planets ($P < 640$ d) (middle), and the theoretical observed planets (right). All populations show strong and significant correlation between the mass of neighbouring planets. This implies that there is a strong likelihood for neighbouring planets to have similar masses. From the perspective of planet formation theory, the trend in mass could be a fundamental trend which also manifests itself in the size correlations.

6.2. Peas in a Pod: Mass

Figure 7 shows the masses of inner and outer planets in an adjacent pair for the underlying population (left), the underlying populations of detectable planets (middle), and KOBE population (right). For the KOBE population, a swapping test as described in Sect. 6.1 was implemented. There is a strong and significant correlation present between the masses of adjacent pairs of KOBE planets. These correlations are also confirmed by the Spearman correlation test. This implies that adjacent planets in the KOBE populations, indeed, have similar masses. Figure 7 also shows that about 55% of KOBE adjacent pairs lie above the $y = x$ line i.e. they are ordered in mass. This means that there are more planetary pairs where the outer planet is also the more massive planet.

Whether this trend is also present in the underlying population is an interesting question. Figure 7 (left and middle) shows that the underlying population have an even stronger and significant mass similarity correlation. In the underlying population, the outer regions of a system are heavily dominated by small planets with $M_{\text{planet}} < 1 M_{\oplus}$. When the population of detectable planets is considered, these small planets are noticeably missing (Fig. 7 (middle)). In addition, mass-ordered adjacent pairs are

more common in the inner region of many planetary systems. Thus, as noted in the last section, considering only detectable planets has two important consequences: increase in mass similarity correlation and increase in frequency of mass-ordered planetary pairs. This suggests that detectable planets in the Bern Model tend to have masses similar to their adjacent neighbour or the outer planet, in an adjacent pair, is often the more massive planet.

Overall, adjacent planets in the KOBE catalogue show mass similarity and ordering. Since mass similarity and ordering are already present in the underlying population of detectable planets, these correlations are not emerging from the detection biases of the transit method. This implies that the peas in a pod: mass similarity and mass ordering trend is probably astrophysical in origin. However, detection biases seem to diminish the strength of these correlations (see Sect. 7).

The patterns seen in the mass trend are strikingly similar to the size trends studied before. This suggests that the two trends may not be independent of each other. This is understandable, since the size of a planet strongly depends on its mass. Planetary mass is evaluated directly from formation physics whereas planetary radius has to be evaluated from additional considerations.

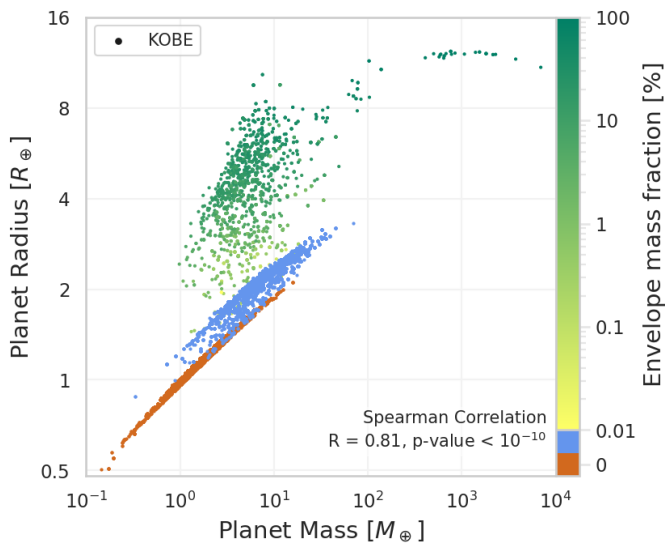


Fig. 8. Mass-radius relationship: The planetary radii is plotted as a function of planetary masses for the planets in the KOBÉ 100 embryo population. For planets with non-zero H/He envelopes, the colour denotes their envelope mass fraction, $\frac{M_{\text{env}}}{M_{\text{planet}}}$. Planets without envelopes and without volatiles in their cores are marked in brown, while planets without envelopes which have volatiles in their cores are marked in blue.

Fig. 8 shows a mass-radius diagram of all planets in the KOBÉ 100 embryo population. Planets with a non-zero envelope mass fraction ($\frac{M_{\text{env}}}{M_{\text{planet}}}$) are marked in yellow-green. Planets without any H/He envelope and without any volatiles in their cores are marked in brown. Planets with no envelope and icy-material in their cores are marked in blue. Planets with large envelope mass fraction are composed mainly of H/He gases which they accreted during their formation. On the other hand, planets with low envelope mass fraction are mostly dominated by their cores and have little H/He gas envelope. The plot shows that Jupiter-sized planets have high envelope mass fractions, while planets with sizes $< 4 R_{\oplus}$ are mostly core-dominated. The high value of the Spearman Correlation coefficient ($R = 0.81$) indicates that the radius as a function of planetary mass is a highly monotonic function¹⁵. This implies that for the KOBÉ planets an increase in planetary mass is very likely to result in an increase in the planetary radius as well.

These factors suggest that the trends of planetary masses are probably more fundamental in the system architecture. The trend seen in the size of adjacent planets is likely to be a derivative trend from the mass correlation.

6.3. Peas in a Pod: Spacing

To investigate the correlation in spacing between adjacent pairs of planets (for systems with 3 or more planets) the ratio of periods are used. Figure 9 shows the period ratio for an outer pair of adjacent planets P_{j+2}/P_{j+1} as a function of the period ratio of an adjacent inner pair of planets P_{j+1}/P_j . Following W18, the period ratios are limited to 4 for the underlying population (left), for underlying population of detectable planets (middle) and for KOBÉ planets (right).

¹⁵ The Spearman Correlation coefficient is unity ($R = 1$) for a strictly monotonic function.

The correlation tests reveals that there is a positive correlation for spacing in the KOBÉ catalogue ($R = 0.25$). The observed CKSM catalogue showed even stronger spacing correlation with $R = 0.46$ (W18). The underlying population shows a much stronger ($R = 0.55$) and significant correlation. This implies that for the theoretically observed and underlying population, the period ratio of one pair of planets is correlated with the period ratio of the next pair of planets. However, this trend is notably diminished when the underlying population is analysed by KOBÉ (discussed further in Sect. 7.2).

The plots in Fig. 9 shows that many pairs of planets are found in mean motion orbital resonances. The dashed horizontal lines are shown to guide the eye for some of the important resonances. The number inside the parenthesis is the percentage of outer planetary pairs which have a period ratio within 1% of the indicated resonance. For example, in the KOBÉ 100 embryo population, about 14% of outer planetary pairs are in the 3/2 orbital resonance. Another 11% and 10% of planetary pairs are captured in 4/3 and 2/1 resonances, respectively. With a period ratio of 1/1, there are also some cases of co-orbital resonances (Leleu et al. 2019).

The spacing correlation increases sharply as the number of embryos increases in the underlying populations (not shown). The introduction of more embryos in a system has several consequences. Most importantly, it increases the dynamical interactions between growing embryos/planets causing more merger collisions and ejection of planets. In addition of creating new planetary neighbours, these scenarios also lead to a dynamical clearing of space. For example, if three consecutive planets in a system have periods 1, 10, and 100 d respectively, then all adjacent pairs have a period ratio of 10. The ejection of the middle planet creates new adjacent pairs with a period ratio of 100. If multiple planets, within a system, are clearing space through dynamical interactions, then this provides a mechanism for adjacent planets with correlated spacing to emerge. In Sect. 8.2, the effects of dynamical interactions are analysed further.

Figure 9 also shows that the frequency of spacing ordered adjacent planetary pairs (i.e. where the period ratio of the outer pair is larger than the inner pair) is always less than 50%. This suggests that it is more common to have larger spacing between the inner pair of planets for any 3 consecutive planets. This frequency decreases with increasing the number of protoplanetary embryos (not shown). This also suggests that increasing dynamical interactions plays a role in allowing adjacent planetary pairs with larger spacings to emerge.

The frequency of ordered adjacent pairs falls sharply for the population of detectable planets. This indicates that, for 3 consecutive planets, an inner pair which has a larger spacing than an outer adjacent pair is much more common in the inner region of a system. This could, potentially, be a result of limited N -body calculation time. In NGPPS, the N -body calculations are done until 20 Myr. This means for a planet located at 1 au or 365 d, the N -body tracks its evolution for 20 M orbits. For planets which are further out, their orbital evolutions are tracked much less and could thereby influence these results.

In the context of spacing between adjacent planets, another possibility to explore is the role played by the initial location of embryos (described in Sect. 3). A simple calculation allows to derive the initial period ratio of embryos by converting uniform log spacing in semi-major axis a_{embryo} to periods.

$$\log \frac{P_{j+1}}{P_j} = \frac{3}{2} \frac{1}{n_{\text{emb}}} \log \left(\frac{a_{\text{embryo}}^{\text{outer}}}{a_{\text{embryo}}^{\text{inner}}} \right) \quad (2)$$

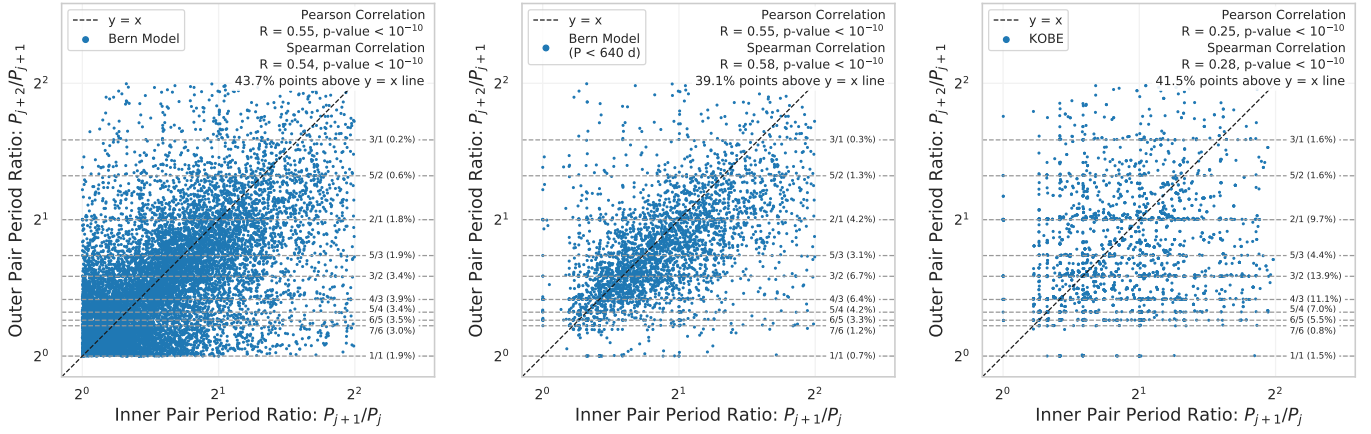


Fig. 9. Peas in a pod - Spacing: For multi-planetary systems with 3 or more planets, the spacing between a pair of adjacent planets is correlated with the spacing between the next pair of planets. The plots show period ratio of outer pair of planets as function of period ratio of inner pair, for the underlying population (left), underlying population of detectable planets (middle), and KOBE systems (right). The underlying populations show strong and significant spacing correlation, while for the KOBE populations this trend is diminished. In addition, all populations show that the spacing for the inner pair is likely to be larger than the spacing of an adjacent outer pair. The dashed horizontal lines mark some of the important resonances. The number inside the parenthesis is the percentage of outer planetary pairs which have a period ratio within 1% of the indicated resonance.

Here, n_{emb} is the total number of embryos initially placed in a simulation and the factor $3/2$ comes from the application of Kepler's third law. $a_{\text{outer}}^{\text{emb}} = 40 \text{ au}$ is the maximum distance from the star at which an embryo can be placed. For the inner edge, the mean value of $r_{\text{in}} = 0.055 \text{ au}$ can be used. This provides an approximate value of the fixed initial period ratio of embryos. The value of this is 1.6, 1.2, and 1.1 for the populations with 20, 50, and 100 embryos respectively. This implies that all planetary embryos start with a fixed period ratio. It is clear from the plot (see also Fig. 12) that there is little trace of these fixed values at 4 Gyr.

Overall, all theoretical populations show a positive spacing correlation in agreement with observations. The spacing between one pair of planets is similar to the spacing between the next pair of planets. The large correlations present in the underlying population suggest that this trend is probably astrophysical in origin. Geometrical limitations and detection biases have a noticeable influence on the spacing correlation (see Sect. 7). For synthetic populations, often, the period ratio of an inner pair of planets is larger than the period ratio of the next outer pair.

6.4. Peas in a Pod: Packing

W18 found that smaller planets tend to have small spacing while larger planets are likely to have large spacing. There was a correlation between the average size of an adjacent planetary pair with their period ratio. The Pearson correlation coefficient for the packing trend in the CKSM catalogue was $R = 0.26$.

It was suggested in Sect. 6.2 that the correlations seen in sizes are probably arising from underlying correlations present in planetary masses. The correlations in planetary masses are probably more fundamental than those of planetary radii. A further test of this idea could be if the packing correlations were to also exist in planetary masses. This has not been reported in the literature before. Figure 10 shows the average size (top) and average mass (bottom) of adjacent pairs of planets as a function of their period ratios P_{j+1}/P_j . The underlying population is shown on the left and the KOBE population is on the right.

For the KOBE population, the Pearson correlation coefficient for the packing trend (with average sizes) is $R = 0.23$, which is in

good agreement with observations. The plot shows that for planetary pairs of average size $1 R_{\oplus}$, the spacing is generally lower as compared to pairs of average size $2 R_{\oplus}$. The correlation stems from the lack of planetary pairs with small average sizes and large spacing between them. Figure 10 (top left) shows that this correlation is even stronger in the underlying population. Here, the correlation coefficient is $R = 0.45$. The plot shows that while there is a cluster of points with low period ratios ($P_{j+1}/P_j < 2$) extending from average sizes 0.5 to $5 R_{\oplus}$, the correlation seems to emerge from the lack of small sized planetary pairs with large spacing. For example, there is only one pair of adjacent planet, in the underlying population, with average size between $1 - 2 R_{\oplus}$ and period ratio between $128 - 512$. For the same period ratio bin, there are 2 pairs of planets with average sizes between $2 - 4 R_{\oplus}$, while there are 8 pairs of planets with average sizes between $4 - 8 R_{\oplus}$.

Figure 10 (bottom) shows that the average mass of planetary pairs is indeed correlated with their spacing. In fact, the correlation of period ratios is stronger with average mass than with average size. The correlation coefficient is $R = 0.26$ for the KOBE population and increases to $R = 0.57$ for the underlying population. These plots show features which are similar in quality to the plots with average sizes. For all populations, there are no planetary pairs with average mass $> 1000 M_{\oplus}$ and spacing $P_{j+1}/P_j < 3/2$. This can be explained by invoking stability arguments. Deck et al. (2013) studied long-term stability of planetary systems and provided stability criterion. The Hill stability criterion (eq. 59 from their paper), relating masses and locations of two planets, is plotted in Fig. 10. A pair of planets are Hill stable if they are on the right side of the black curve.

To further understand the packing trend, the location of the inner planet (in an adjacent pair) is marked in colour for the underlying population. The coloured plots show several interesting features. This trend is mostly driven by planetary pairs where the inner planet is located close to the host star ($P \lesssim 10 \text{ d}$). For these pairs of planets, the spacing seems to increase with their average size/mass.

As mentioned in Sect. 6.3, dynamical interactions can lead to merger collisions and ejection of planets. This results in dynamical clearing of space between planets. Large planets may un-

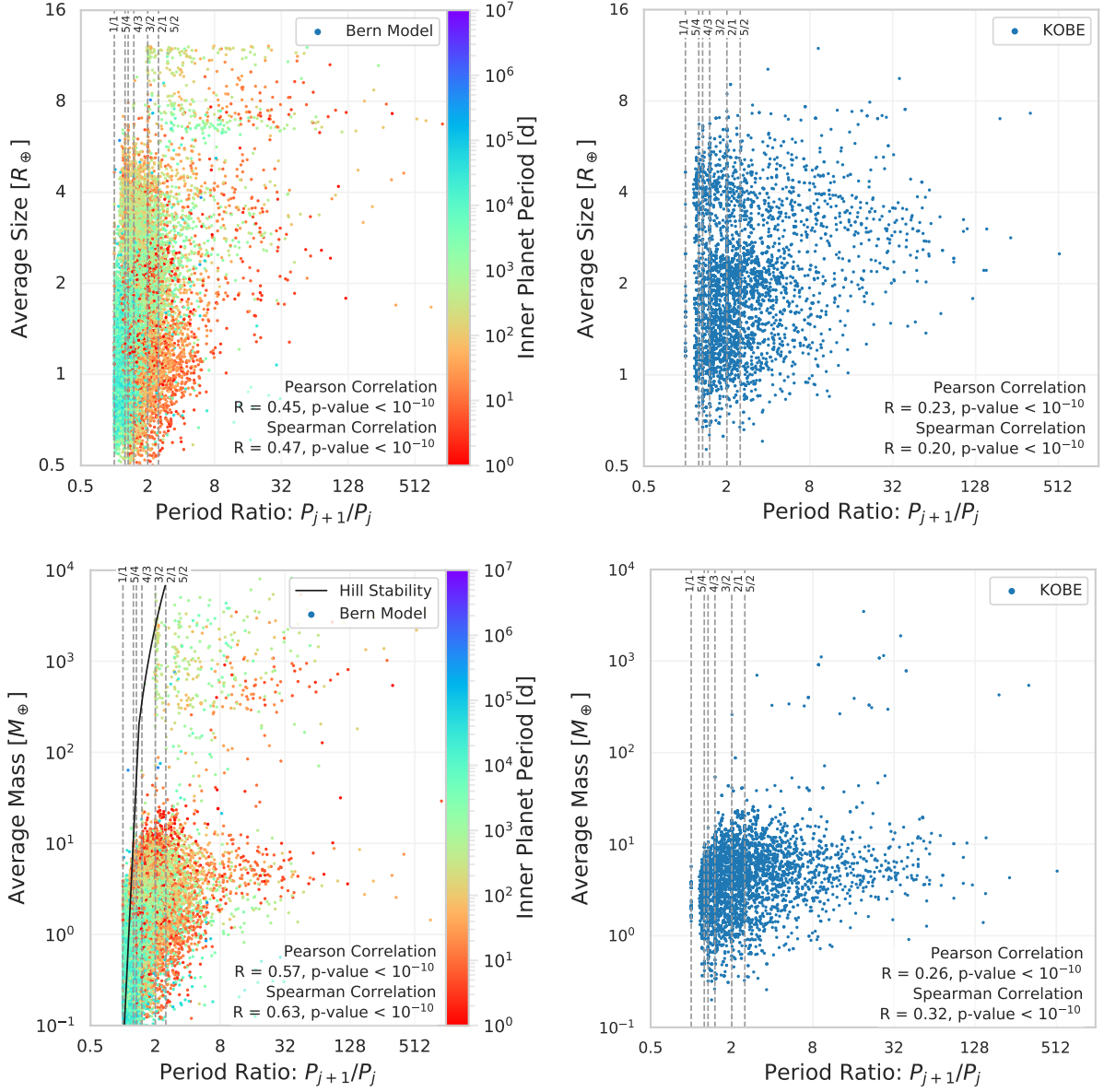


Fig. 10. Peas in a pod - Packing: The average sizes (top) and average masses (bottom) of adjacent planets are shown as a function of their orbital period ratios P_{j+1}/P_j for the underlying population (left) and KOBE planets (right). The correlation tests confirm that the average masses (and therefore average sizes) of planetary pairs are correlated with their spacing. The correlations are even stronger in the underlying population. It is suggested that the packing trend in terms of planetary masses is more fundamental than the packing trend in terms of planetary sizes. For the underlying population, the position of the inner planet in each pair is marked with a colour. This shows that the trend is due to those planetary pairs where the inner planet is close to the host star. The black curve in the bottom left shows the Hill stability criterion from [Deck et al. \(2013\)](#). Adjacent planetary pairs on the right side of this curve are Hill stable. Points on the left side are Hill unstable and will probable be removed with longer N-body calculations.

dergo several collisions leading to the ejection/accretion of several planets. This may allow them to have wider orbital spacing. On the contrary, small planets may not have undergone several collisions, thereby remaining in compact configurations. This could explain how small planets tend to have smaller orbital spacing and large planets have wider orbital spacing. Due to limited N -body integration time, the inner region (< 1 au/365 d) of a planetary system experiences much more dynamical interactions as compared to the outer region. This explains the small contribution towards the packing trend from planets which are in the outer region (i.e. green points). This scenario is discussed further in Sect. 8.2.

Overall, the findings of this section indicate that the average mass (and therefore the average size) of a planetary pair is correlated with their spacing. Planets with smaller masses are packed closely together while massive planets seem to have larger orbital spacing between them. As these correlations are also present in the underlying population, it hints towards an astrophysical origin of this trend. In [W18](#), this trend was further examined through the mutual separation (Δ) of adjacent planet in units of mutual Hill radius. Their findings can be explained by detection biases and is discussed in appendix A.

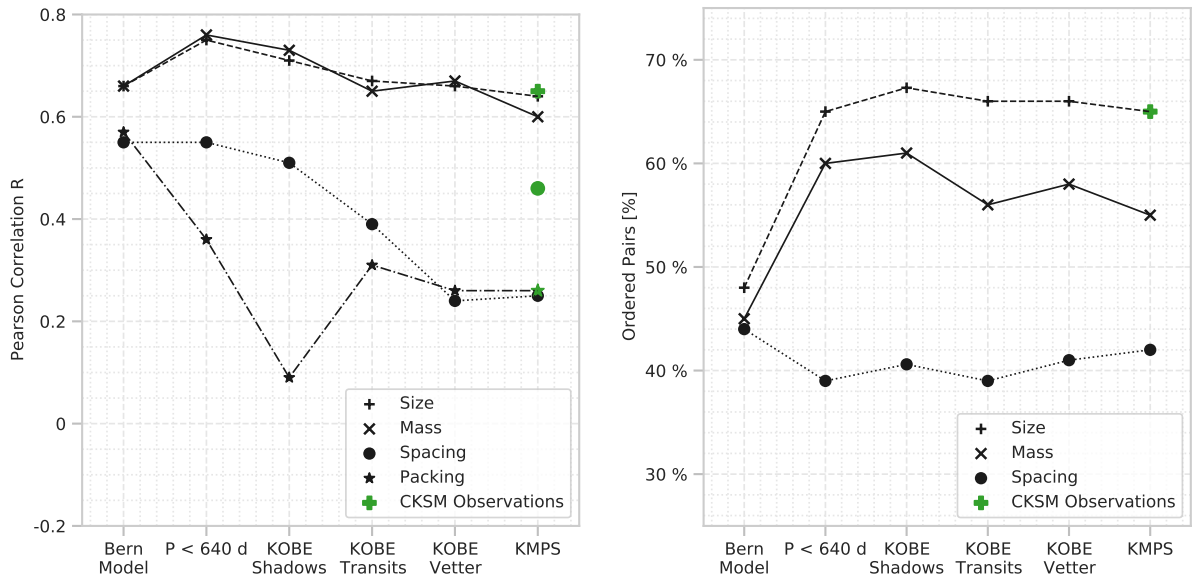


Fig. 11. The influence of the geometrical limitations of the transit method (KOBE-Shadows), the transit detection biases (KOBE-Transits), and the completeness of the Kepler survey (KOBE-Vetter) on the peas in a pod trend. The plot shows how the correlation coefficients (left) and the frequency of ordered pairs (right) varies in the underlying Bern Model population, underlying population of detectable planets ($P < 640$ d), and the theoretically observed KOBE population. Observations from the CKSM exoplanetary catalogue are marked in green.

7. Role of detection biases on peas in a pod trend

Due to the geometrical limitations and detection biases inherent in the transit method, our knowledge of nature’s underlying exoplanetary populations is incomplete. When a trend in the architecture of observed exoplanetary population emerges, it is, therefore, unclear whether this trend reflects an actual property of nature or is simply an outcome of our incomplete knowledge of nature’s exoplanetary population.

In W18 the origins of the peas in a pod trend was investigated using ‘null hypothesis’ bootstrap tests. The basic idea behind these tests was that if detection biases of the transit method are responsible for the observed trends, then these correlations should also be present in a ‘mock’ exoplanetary population which does not possess these trends inherently through a null hypothesis but suffers from the same detection biases. Weiss & Petigura (2020) state their null hypothesis as: the size of a planet is random and independent of the size of its neighbour. For the spacing trend their null hypothesis is: the orbital period ratio between one pair of planets is not, a priori, related to the orbital period ratio of the next pair of planets in the same system (W18). They performed 1 000 bootstrap trials in which the detection biases of Kepler was applied to mock populations satisfying the null hypothesis stated above. They found that none of their bootstrap trials could lead to a population which had the peas in a pod trends. Since the detection biases convolved with the null hypothesis did not result in the peas in a pod trend, they concluded that these trends are not due to detection biases and must be of astrophysical origin. Their method was extensively challenged by Zhu (2020). Different null hypothesis are studied by Murchikova & Tremaine (2020).

Population synthesis based on planet formation models provides a natural playground for testing these trends. The Bern Model consists of theoretical description for many physical phenomenon that are active during planet formation. Supplying them with randomized initial conditions and N -body calculations, the NGPPS provides a theoretical version of nature’s underlying population. The KOBE catalogue, from KOBE, stands on

the same footing as observations (CKSM). This work, hence, allows both the theoretically observed exoplanetary populations (from KOBE) and the theoretical underlying populations (from NGPPS) to be investigated for the peas in a pod trend. As the underlying populations are available, a null hypothesis based bootstrap testing procedure is not required.

To understand how the geometrical limitations and the detection biases of the transit method affect the peas in a pod trends, the correlation test was performed after each stage of calculations in KOBE. Figure 11 (left) shows the Pearson correlation coefficient for the similarity trends in size, mass, spacing, and packing. Going from left to right, the 100 embryos populations on the x-axis are: underlying Bern Model, underlying Bern Model population of detectable planets ($P < 640$ d), KOBE-Shadows catalogue (with geometrical limitations of the transit method), KOBE-Transits catalogue (with detection biases), KOBE-Vetter catalogue (accounting for Kepler’s completeness and reliability), and KOBE multi-planetary systems (KMPS) (same cuts as W18’s CKSM). Figure 11 (right) shows the percentage of ordered pairs for size, mass and spacing for the same populations¹⁶. Observations from CKSM are marked in green.

The similarity and the differences of these trends can be understood with the following statement: *The chances of detecting a transiting exoplanet depend strongly on its location (star-planet distance/orbital period) and weakly on its size (radius).* Specifically, the size dependence is from $R_{\text{planet}}/R_{\star}$ (see eq. C.6) which varies from 10^{-3} for sub-Earth-size planets to 10^{-1} for Jupiter-Size planets around a Sun-like star. This suggests that the effect of geometrical limitations and detection biases will be much more severe on orbital periods than on planetary sizes. This is easily seen from the plots in Fig. 2 and Fig. 11.

¹⁶ An ordered pair is one in which the outer planet (from the star) has the larger value for a given quantity (radius, mass, etc.).

7.1. Peas in a pod: Mass & Size

One striking feature from Fig. 11 is that the size trend closely follows the mass trend. The small variations between the two trends are probably arising from the scatter seen in the mass-radius diagram (see Fig. 8). The underlying population shows strong mass (and thereby size) similarity and ordering correlations. This strongly indicates that the peas in a pod mass (and thereby size) trend is arising from planet formation.

The geometrical limitations and detection biases of the transit method tend to decrease the strength of the similarity correlations. The vetting procedure, in KOBE-Vetter, seems to have little effect on the mass (size) similarity correlations. Although the completeness of Kepler's Robovetter drops sharply with radius (see Fig. C.2), the frequency of large planets in the KOBE-Vetter catalogue is also low – about 70% of planets have $R_{\text{planet}} \leq 3 R_{\oplus}$. Finally, the size correlations seen in the KMPS catalogue match very well with observations.

However, KOBE has little influence on the mass/size ordering trend. For the underlying population of detectable planets, the frequency of mass/size ordered pairs is close to 60%. This means that there is a higher chance for an outer planet in a pair to be heavier/larger. The frequency of size-ordered pairs in KOBE matches very well with CKSM observations.

Since the size similarity and ordering trend in the KOBE populations matches very well with observations, one could extrapolate this to learn about nature's underlying exoplanetary population. These results suggest that the size/mass similarity and ordering correlations found in observations are probably astrophysical and are not severely affected by detection biases.

7.2. Peas in a pod: Spacing & Packing

The underlying populations shows strong spacing (for systems with 3 or more planets, period ratios limited to 4) and packing trends. Both of these trends involve period ratios of adjacent planets, already hinting that these trends will be strongly influenced by KOBE. One way in which KOBE influences the spacing and packing trends is due to missing planets.

KOBE-Shadows finds transiting planets, which have a fortuitous alignment with an observer. Transiting planets, found by KOBE-Shadows, are not necessarily consecutive. In several cases, many intermediate planets are missed resulting in a strong affect on period ratios. However, the effect of missing planets may be more adverse on the packing trend than on the spacing trend. Consider a hypothetical system with 5 planets at periods of 1, 10, 100, 1 000, and 10 000 d. The period ratio for all four adjacent pairs is 10, and the ratio of period ratios for any 3 consecutive planet is 1. If the planets with periods of 10, and 1 000 d do not transit for an observer, then the period ratios of the two transiting adjacent pairs jumps to 100. However, for the three transiting planets, the ratio of their period ratio is still 1. If the two transiting adjacent planets have small average sizes, then the jump in the period ratio will weaken the packing correlation. This example demonstrate the adverse effect of missing planets on the packing trend¹⁷. This explains the diminishing of the spacing trend and the absence of packing correlation from the 100 embryo population in the KOBE-Shadows catalogue.

¹⁷ Each stage of KOBE's calculation introduces some randomness (location of observers, or vetting planetary candidates). Even if all planets in a system were to be in the same orbital plane, the randomness inherent in KOBE's calculation or the variation in their sizes could lead to "random" missing planets.

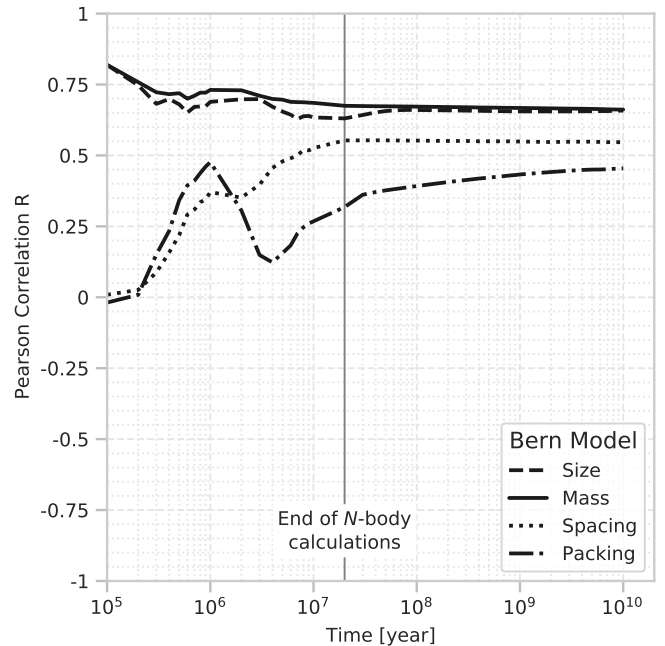


Fig. 12. The evolution of the peas in a pod trends. The vertical solid line represents the end of N -body calculations. The plot shows that dynamical interactions during the formation stage play a vital role in shaping the architecture of planetary systems. While the size/mass trends are present at very early times, the spacing and packing trends are almost absent at early times.

KOBE-Transits requires that all transiting planets have at least 2 transits, which implies that only planets with $P < 640$ d can be included. This means that only the inner region of a planetary system is now considered. This helps in removing pairs with abnormally large period ratios caused by missing planets. This may explain how the packing trend is restored in the catalogue from KOBE-Transits. The spacing trend is reduced further by KOBE-Transits and KOBE-Vetter. These modules provide imprints of the physical detection biases and completeness profile of the Kepler pipeline.

The role of adding biases on the spacing ordering trend can be seen from Fig. 11 (right). For the underlying population, the frequency of ordered pairs is less than 50% (for 3 consecutive planets, there are more inner pairs with larger spacing than their next outer pair). There seems to be little influence of KOBE, and thereby detection biases, on the frequency of ordered pairs.

Overall, the underlying populations show strong spacing and packing trend. Geometrical limitations and detection biases of the transit method are responsible for reducing the strength of these correlations.

8. Discussion – Theoretical Scenarios

Results of Sect. 6 indicate that the peas in a pod trend is present in the synthetic planetary systems from the Bern Model. This section is dedicated to the discussion of some theoretical scenarios that offer partial explanations for these trends.

8.1. The evolution of peas in a pod

One way to understand how the peas in a pod trends emerge is by investigating when the trends emerge. For this, the correlation

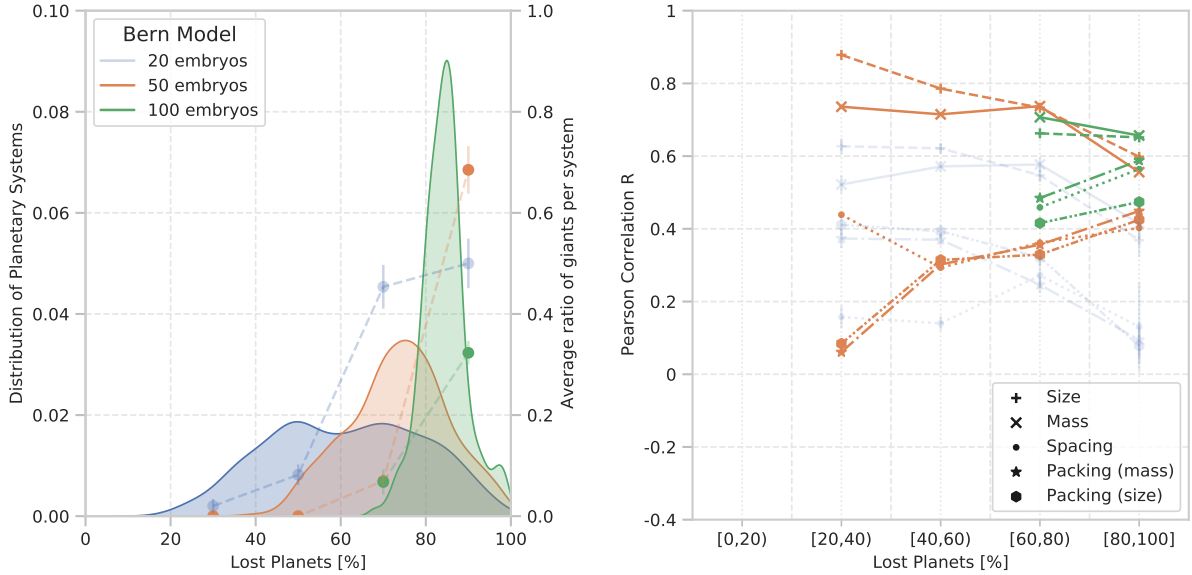


Fig. 13. The role of dynamical interactions on the peas in a pod trends. Left: The plot shows the distribution of lost planets [%] by systems in the 20, 50 and 100 embryo NGPPS populations. The fraction of planets lost by a system can be used as a proxy for the cumulative dynamical interactions experienced by a system. The dashed lines show the ratio of giant planets per system averaged over bins. Right: The correlation coefficient for the peas in a pod trends are shown for each bins. The error bars correspond to the standard error of the correlation coefficient (Zar 2014). Increasing dynamical interactions results in the strengthening of the spacing and packing trend.

tests for all trends was performed for all underlying populations at all time steps. Figure 12 shows the evolution of the correlation coefficients for the underlying 100 embryo population. The solid and dashed lines represent the Pearson R correlation coefficients for the mass and size similarity trends, respectively. The dotted and dash-dotted lines represent the correlation for spacing (period ratios limited to 4) and packing (with average size), respectively. The vertical black line indicates the end of N -body calculations at 20 Myr. This serves to qualitatively divide the plot into a planet formation stage (left) and thermodynamical evolutionary stage (right). Since most of the variations happen during the N -body calculations, this suggests that dynamical interactions during the formation stage play a key role in shaping these trends.

The plot shows that the underlying population shows a very strong correlation for the size and mass trends, already at the beginning of the calculations. This suggests that the peas in a pod mass (and thereby size) similarity trends are present at very early times. This high correlation can be attributed to two factors: oligarchic growth of protoplanetary embryos and uniform accretion of solids by protoplanets at early times (see Sect. 2.2). The Bern Model starts with lunar mass embryos which are separated by at least $10 R_H$. Runaway growth of planetesimals leads to protoplanets, which eventually grow oligarchically. The oligarchic growth stage results in mass ratios approaching unity (Kokubo & Ida 1998). In this way, the seeds for the peas in a pod mass trend (and therefore also the size trend) is already planted. In the Bern Model, protoplanetary embryos accrete solids from the planetesimal disk at a rate given by eq. B.6. This core accretion rate prominently depends on the location and mass of the embryo as well as the surface density of the disk, Σ_s . Since these factors (surface density of solid disk and location/mass of embryos) do not undergo any drastic changes at early times, the accretion of solids by neighbouring protoplanets is uniform. Thus, uniformly growing oligarchic embryos may explain the high mass/size correlation seen at $t = 10^5$ yr in Fig. 12.

Between $t = 10^5 - 10^6$ yr the correlation coefficient for mass (and thereby size) drops. This could be attributed to the differences in the rate of solid accretion by cores of different types of planets. The cores of giant planets have to reach a critical mass ($M_{\text{core}} \approx 10 - 20 M_{\oplus}$) before the gas disk dissipates (Pollack et al. 1996; Alibert et al. 2005). On the other hand, planetary cores which will fail to reach this critical mass (for runaway gas accretion), are known to have longer formation times (Paper I). If adjacent planetary cores in a system would grow at different rates, the correlation between their masses/sizes may decrease. The size correlation seems to trace the mass correlation (with some scatter). That the size trend follows the mass trend is not surprising, since planetary sizes are calculated from their masses (via internal structure calculations).

Between $t = 10^6 - 2 \times 10^7$ yr the correlation coefficient for mass decreases slightly. Most giant planets would have acquired their final masses in the first few Myrs. Other planets, however, continue to grow by solid accretion, gas accretion (before the gas disk dissipates), and merger collisions. This implies that adjacent neighbours may be growing at different rates depending on their local environment. Different growth rates implies that the mass correlation will decrease. The local environment around planets growing in the same disk does not suffer any drastic changes. This may explain why the mass correlation does not show any drastic changes as well. Additionally, the dissipation of gas disk has a strong effect on planetary radii, since planets contract rapidly after disk dispersal. This may contribute to the decreasing size correlation in this time period.

The spacing and packing trends start with almost no correlation and undergo interesting variations before ending with their final value. Initially, adjacent planets have uncorrelated small period ratios and small sizes. This may explain the absence of these trends at early times. Some physical processes which affects the location of a planet are orbital migration, resonance capture and ejection/collision of planets. When a planet is lost (via ejection or collision), it clears up space allowing new adja-

cent pairs to emerge with wider orbital spacing. This dynamical sculpting may explain how planets within a system evolve towards similar spacing. Large-sized planets may undergo several collisions which leads to the ejection of several planets allowing them to have wider spacings. This offers a possible explanation for the emergence of the packing trend. After a few Myrs, most systems are losing their gas disks, which leads to rapid contraction of planetary radii. This is responsible for the sharp drop in packing trend (between $t = 10^6 - 2 \times 10^7$ yr). As planets continue to grow via merger collisions, the packing trend re-emerges slowly.

The spacing and packing trends are seen to have several common behaviour. They are both absent at early times, arise from dynamical interactions and are strongly influenced by the detection biases. It is a possibility that these two trends are not independent of each other. In fact there exists a simple scenario which could unify them: The peas in a pod spacing trend could be a reflection of the mass-similarity and the packing trends. Since adjacent planets are more likely to have similar masses, and the orbital spacing between planetary bodies is related to their masses (heavy planets have wider orbital spacing, while small planets tend to have smaller orbital spacing), the spacing trend can emerge. Planets with large/small masses have neighbours with similar masses, and this leads them to have period ratios which are also similar. Further tests are required to confirm this scenario.

Overall, this section has two important findings:

1. The similarity in mass/size trends are already present at early times. These are due to oligarchic growth of protoplanetary embryos and uniform growth of these protoplanets at early times. Uniformly growing neighbouring planets will continue to show size/mass similarity. Different growth rates amongst adjacent planets, during the formation stage, tends to decrease the mass/size trends.
2. The spacing and packing trends are absent at early times. Dynamical interactions (especially merger collisions) tend to increase spacing and packing correlations.

8.2. Role of Dynamical Interactions

Dynamical interactions can often lead to ejection of planets and merger collisions. This would lead to a decrease in the number of planets in a system. Systems which have had more dynamical interactions will have lost more planets than systems with less dynamical interactions. Since, the number of embryos (n_{emb}) that a theoretical system begins with is fixed for each synthetic population, the percentage of lost planets can be used as a diagnostic for its dynamical history. With n_{mul} as the multiplicity of systems at 4 Gyrs, the percentage of planets lost by a system is:

$$\text{Lost planets } [\%] = \frac{n_{\text{emb}} - n_{\text{mul}}}{n_{\text{emb}}} \times 100. \quad (3)$$

Figure 13 (left) shows the distribution of lost planets in the underlying NGPPS populations. This plot shows that the distribution shifts to the right, as the number of embryos increases from 20, 50 to 100. This demonstrates that adding more embryos in a system tends to increase their dynamical interactions which, in turn, forces these systems to lose more planets. This verifies that lost planets can be used as a proxy for the dynamical interactions experienced by a system.

Now, planetary systems are divided into 5 sub-populations depending on the percentage of planets they lost: [0,20), [20-40), [40-60), [60-80), and [80-100]. The ratio of giant planets to

the total number of planets in each system is calculated¹⁸. This ratio is then averaged over each sub-population and is shown in Fig. 13 (left). There is clear increase in the ratio of giant planets, in a system, with increasing dynamical interactions. This shows that systems with more giant planets have more cumulative dynamical interactions.

For each peas in a pod trend (size, mass, spacing, and packing), the correlation coefficient is measured across each sub-population. This is shown in Fig. 13 (right). As the percentage of lost planets increases, the spacing and packing correlations also increase (for the 50, and 100 embryo populations). This strongly suggests that increasing dynamical interactions results in strengthening of the spacing and the packing trends. This adds support to the finding of the last section that dynamical interactions amongst growing planets leads to the spacing and packing trend. For the 20 embryo population, the result of the Pearson correlation test becomes unreliable due to low multiplicities. Going from left to right, the size/mass correlations show little variations at first. However, the size/mass correlations drop sharply in the last 2 bins. This drop may arise from the presence of giant planets in these sub-population, indicating an anti-correlation between mass similarity and presence of giant planets.

9. Summary, Conclusions and Future works

In this paper, the peas in a pod trends in the architecture of planetary system is studied. Using the Bern Model, thousands of synthetic planetary systems were simulated. To compare this population of theoretical systems with observations, a new computer code, KOBE, was developed and is introduced in this paper.

KOBE closely simulates the geometrical limitations of the transit method and the detection biases of the Kepler transit survey. KOBE-Shadows finds transiting planets via their transit shadow bands, thereby imprinting the transit probability and including the geometrical limitations of the transit method. By selecting only high SNR transiting planets, as calculated by KOBE-Transits, the detection biases of the Kepler mission are simulated. Finally, KOBE-Vetter rejects some of the planets as false positives, emulating the completeness and reliability of the Kepler Robovetter. Transiting planets that are dispositioned as planetary candidates make up the KOBE catalogue.

Additional selections cuts are placed on the KOBE catalogue to generate the KOBE multi-planetary systems population. This population is compared with the multi-planetary systems catalogue of the California-Kepler Survey (CKSM from W18). The KOBE and CKSM planetary populations showed similar radius and period distributions. The peas in a pod trend was investigated for several populations.

The main conclusions of this paper are:

1. Similarity in Size/Mass

The peas in a pod: size and mass similarity trends are present in the theoretically observed (KOBE) and the theoretical underlying (Bern Model) populations. This means that adjacent planets within a system tend to have similar sizes/masses. The strength of the size trend in the KOBE population is in good agreement with observations. Detection biases tend to diminish the strength of these correlations.

2. Ordering in Size/Mass

The peas in a pod: size and mass ordering trend is present in the theoretically observed (KOBE) population. The frequency

¹⁸ Following Paper II, giant planets are defined as planets with $M_{\text{planet}} \geq 300M_{\oplus}$.

of size-ordered pairs is in good agreement with observations. This trend is also present in the theoretical underlying population of detectable planets (planets with periods less than 640 days). Thus, in the inner region of a system there is a higher chance for an outer planet in an adjacent pair to be larger/more massive. Detection biases of the transit method have little influence on this trend.

3. The peas in a pod mass/size trends are present at very early times. The primordial origin of these trends is due to oligarchic growth of protoplanetary embryos and the uniform growth of planets at early times. Later stage of planet formation, including dynamical N -body effects, allows planets within a system to grow at different rates. This tends to decrease the strength of these trends.

4. Peas in a pod: Spacing

In the peas in a pod: spacing similarity trend, for 3 consecutive planets in a system, the period ratio of the inner pair tends to be similar to the period ratio of the outer pair. This correlation is present in the theoretically observed (KOBE) and the theoretical underlying (Bern Model) populations.

5. This trend is absent at early times and likely arises from the dynamical interactions taking place during planet formation stage. Merger collisions and ejection of planets are some of the ways through which planets become evenly spaced. Additionally, this trend increases when the number of embryos in a population is increased, further suggesting that dynamical interactions increase this trend.
6. The strength of this trend is higher in the underlying population. Detection biases are responsible for reducing the strength of these correlations.

7. Peas in a pod: Packing

Observations suggest that large planets tend to have wider orbital spacing, while small planet are often packed in compact configurations. This packing trend is also present in theoretically observed (KOBE) and the theoretical underlying (Bern Model) catalogues. The strength of this trend is in good agreement with observations.

8. This trend is not present at early times and probably arises from N -body dynamical interactions. Large planets undergo several merger collisions, thereby clearing more space around them.
9. Detection biases and missing intermediate planets have a strong influence on this trend. These effects tend to diminish these correlations.

10. Unification

The peas in a pod size trends are probably derivative of the peas in a pod mass trends. The existence of mass trends is probably an astrophysical phenomenon. It has also been suggested that the mass-similarity and packing trend may combine to give rise to the spacing trend.

The results of this paper imply that physical processes involved in planet formation gives rise to adjacent planets which have similar masses (and therefore sizes), and are evenly spaced. Large planets tend to have wider orbital spacing, while smaller planets tend to be packed in compact configurations. Detection biases of the transit method diminish the size/mass similarity trends but have little influence on the spacing and packing trend. This suggests that the peas in a pod similarity and ordering trends, seen in observations, may have an astrophysical origin.

One of the shortcoming of this and other studies on the peas in a pod trends is the usage of correlation coefficients in measuring architecture trends. Although useful in making population-level studies, reliable calculation of correlation coefficients requires large datasets which hinder the study of these trends at the

system level. One line of future work could be the development of system level architecture metrics (Alibert (2019); Mishra et al. (2019); Gilbert & Fabrycky (2020)). These metrics could allow the architecture of an individual system, the solar system for example, to be studied. This could allow the disentanglement of the role played by specific initial conditions from the effects of planet formation processes in engendering these trends. Furthermore, system level studies are required to establish the unification of peas in a pod trends, as mentioned previously.

In addition, the present study can be improved by studying different stellar types. To facilitate comparison with W18, several aspects of KOBE were restricted in this paper. For example, the calculation of transit SNR in KOBE assumes that all planets are in circular orbits, the sampling of CDPP used fixed value of $t_{\text{trial}} = 6h$. Future version of KOBE will include the effect of eccentricity on transit SNR, and will use t_{trial} values based on calculated transit durations. Additionally, KOBE can be further improved by including stellar limb darkening.

Acknowledgements. This work has been carried out within the framework of the NCCR PlanetS supported by the Swiss National Science Foundation. The authors acknowledge support from the Swiss National Science Foundation under grant BSSGI0_155816 “PlanetsInTime”. A.E. acknowledges the support from the University of Arizona. Calculations were performed on the Horus cluster at the University of Bern.

Data: The synthetic planetary populations (NGPPS) used in this work are available online at <http://dace.unige.ch> under section “Formation & evolution”. This research has made use of the NASA Exoplanet Archive, which is operated by the California Institute of Technology, under contract with the National Aeronautics and Space Administration under the Exoplanet Exploration Program: <https://exoplanetarchive.ipac.caltech.edu> (DOI: 10.26133/NEA6). The CKS dataset is available at <https://california-planet-search.github.io/cks-website/>.

Software: KOBE (this paper), Python (Van Rossum & Drake 2009), NumPy (Oliphant 2006), SciPy (Virtanen et al. 2020), Seaborn (Waskom & the seaborn development team 2020), Pandas (pandas development team 2020), Matplotlib (Hunter 2007).

ORCID iDs

Lokesh Mishra	0000-0002-1256-7261
Yann Alibert	0000-0002-4644-8818
Adrien Leleu	0000-0003-2051-7974
Alexandre Emsenhuber	0000-0002-8811-1914
Christoph Mordasini	0000-0002-1013-2811
Remo Burn	0000-0002-9020-7309
Stéphane Udry	0000-0001-7576-6236
Willy Benz	0000-0001-7896-6479

References

- Adams, F. C. 2019, MNRAS, 488, 1446
 Adams, F. C., Batygin, K., Bloch, A. M., & Laughlin, G. 2020, MNRAS, 493, 5520
 Alibert, Y. 2019, A&A, 624, A45
 Alibert, Y., Carron, F., Fortier, A., et al. 2013, A&A, 558, A109
 Alibert, Y., Mordasini, C., & Benz, W. 2004, A&A, 417, L25
 Alibert, Y., Mordasini, C., & Benz, W. 2011, A&A, 526, 1
 Alibert, Y., Mordasini, C., Benz, W., & Winisdoerffer, C. 2005, A&A, 434, 343
 Armstrong, D. J., Lopez, T. A., Adibekyan, V., et al. 2020, Nature, 583, 39
 Baillié, K., Marques, J., & Piau, L. 2019, A&A, 624, 1
 Baraffe, I., Homeier, D., Allard, F., & Chabrier, G. 2015, A&A, 577, A42
 Barnes, J. 2007, PASP, 119, 986
 Benz, W., Ida, S., Alibert, Y., Lin, D., & Mordasini, C. 2014, in Protostars and Planets VI, ed. H. Beuther, R. Klessen, C. Dullemond, & T. Henning (University of Arizona, Tucson), 691–713
 Borucki, W. J. 2016, Reports on Progress in Physics, 79
 Borucki, W. J., Koch, D., Basri, G., et al. 2010, Science, 327, 977
 Borucki, W. J., Koch, D. G., Basri, G., et al. 2011, ApJ, 736, 19
 Borucki, W. J. & Summers, A. L. 1984, Icarus, 58, 121
 Brügger, N., Alibert, Y., Ataiee, S., & Benz, W. 2018, A&A, 619, A174

- Brügger, N., Burn, R., Coleman, G. A. L., Alibert, Y., & Benz, W. 2020, *A&A*, 640, A21
- Bryson, S., Coughlin, J., Batalha, N. M., et al. 2020, *AJ*, 159, 279
- Burrows, A., Hubeny, I., Budaj, J., & Hubbard, W. B. 2007, *ApJ*, 661, 502
- Chambers, J., Wetherill, G., & Boss, A. 1996, *Icarus*, 119, 261
- Chambers, J. E. 1999, 304, 793
- Christiansen, J. L., Jenkins, J. M., Barclay, T. S., et al. 2012, *PASP*, 124, 1279
- Ciardi, D. R., Fabrycky, D. C., Ford, E. B., et al. 2013, *ApJ*, 763, 41
- Clarke, C. J., Gendrin, A., & Sotomayor, M. 2001, 328, 485
- Coleman, G. A. & Nelson, R. P. 2014, 445, 479
- Coughlin, J. L. 2017, KSCI-19114-001, 1
- Deck, K. M., Payne, M., & Holman, M. J. 2013, *ApJ*, 774, 129
- Demory, B. O., Gillon, M., De Wit, J., et al. 2016, *Nature*, 532, 207
- Dittkrist, K. M., Mordasini, C., Klahr, H., Alibert, Y., & Henning, T. 2014, *A&A*, 567 [arXiv:1402.5969]
- Emsenhuber, A., Mordasini, C., Burn, R., et al. 2020a, arXiv e-prints, arXiv:2007.05561
- Emsenhuber, A., Mordasini, C., Burn, R., et al. 2020b, arXiv e-prints, arXiv:2007.05562
- Espinoza, N., Brahm, R., Henning, T., et al. 2020, 491, 2982
- Evans, T. M., Sing, D. K., Wakeford, H. R., et al. 2016, *ApJ*, 822, L4
- Fabrycky, D. C., Lissauer, J. J., Ragozzine, D., et al. 2014, *ApJ*, 790, 146
- Flaherty, K., Hughes, A. M., Simon, J. B., et al. 2020, *ApJ*, 895, 109
- Fortier, A., Alibert, Y., Carron, F., Benz, W., & Dittkrist, K.-M. 2013, *A&A*, 549, A44
- Fulton, B. J., Petigura, E. A., Howard, A. W., et al. 2017, *AJ*, 154, 109
- Gilbert, G. J. & Fabrycky, D. C. 2020, *AJ*, 159, 281
- Guillot, T. 2010, *A&A*, 520, 1
- Hadden, S. & Lithwick, Y. 2017, *AJ*, 154, 5
- He, M. Y., Ford, E. B., & Ragozzine, D. 2019, 490, 4575
- Heng, K. 2019, 490, 3378
- Hoeijmakers, H. J., Ehrenreich, D., Heng, K., et al. 2018, *Nature*, 560, 453
- Hsu, D. C., Ford, E. B., Ragozzine, D., & Morehead, R. C. 2018, *AJ*, 155, 205
- Hueso, R. & Guillot, T. 2005, *A&A*, 442, 703
- Hunter, J. D. 2007, *Computing in science & engineering*, 9, 90
- Ida, S. & Lin, D. N. C. 2004, *ApJ*, 616, 567
- Jin, S., Mordasini, C., Parmentier, V., et al. 2014, *ApJ*, 795, 65
- Johansen, A., Oishi, J. S., Low, M. M. M., et al. 2007, *Nature*, 448, 1022
- Johnson, J. A., Petigura, E. A., Fulton, B. J., et al. 2017, *AJ*, 154, 108
- King, A. 2009, *As*, 500, 53
- Kipping, D. 2018, 473, 784
- Kipping, D. M. & Sandford, E. 2016, 463, 1323
- Kley, W. & Dirksen, G. 2006, *A&A*, 447, 369
- Kokubo, E. & Ida, S. 1998, *Icarus*, 131, 171
- Kokubo, E. & Ida, S. 2002, *ApJ*, 581, 666
- Kreidberg, L., Bean, J. L., Désert, J. M., et al. 2014, *Nature*, 505, 69
- Leleu, A., Coleman, G. A. L., & Ataiee, S. 2019, *A&A*, 631, A6
- Lissauer, J. J., Ragozzine, D., Fabrycky, D. C., et al. 2011, *ApJS*, 197, 8
- Lodders, K. 2003, *ApJ*, 591, 1220
- Lüst, R. 1952, *Zeitschrift Naturforschung Teil A*, 7, 87
- Lynden-Bell, D. & Pringle, J. E. 1974, 168, 603
- MacDonald, M. G., Dawson, R. I., Morrison, S. J., Lee, E. J., & Khandelwal, A. 2020, *ApJ*, 891, 20
- Manara, C. F., Mordasini, C., Testi, L., et al. 2019, *A&A*, 631, L2
- Marboeuf, U., Thiabaud, A., Alibert, Y., Cabral, N., & Benz, W. 2014, *A&A*, 570 [arXiv:1407.7271]
- Matsuyama, I., Johnstone, D., & Murray, N. 2003, *ApJ*, 585, L143
- Mayor, M. & Queloz, D. 1995, *Nature*, 378, 355
- Millholland, S., Wang, S., & Laughlin, G. 2017, *ApJ*, 849, L33
- Mishra, L., Alibert, Y., & Udry, S. 2019, in *EPSC-DPS Joint Meeting 2019*, Vol. 2019, EPSC-DPS2019-1616
- Mordasini, C. 2018, *Planetary Population Synthesis*, ed. H. J. Deeg & J. A. Belmonte, 143
- Mordasini, C., Alibert, Y., Benz, W., Klahr, H., & Henning, T. 2008, PhD thesis
- Mordasini, C., Alibert, Y., Benz, W., Klahr, H., & Henning, T. 2012a, *A&A*, 541, A97
- Mordasini, C., Alibert, Y., Benz, W., & Naef, D. 2009, *A&A*, 501, 1161
- Mordasini, C., Alibert, Y., Georgy, C., et al. 2012b, *A&A*, 547, A112
- Mordasini, C., Alibert, Y., Klahr, H., & Henning, T. 2012c, *A&A*, 547, A111
- Mordasini, C., Marleau, G. D., & Mollière, P. 2017, *A&A*, 608 [arXiv:1708.00868]
- Mordasini, C., Mollière, P., Dittkrist, K.-M., Jin, S., & Alibert, Y. 2015, *International Journal of Astrobiology*, 14, 201
- Mulders, G. D., Mordasini, C., Pascucci, I., et al. 2019, *ApJ*, 887, 157
- Mulders, G. D., O'Brien, D. P., Ciesla, F. J., Apai, D., & Pascucci, I. 2020
- Mulders, G. D., Pascucci, I., Apai, D., & Ciesla, F. J. 2018, *AJ*, 156, 24
- Murchikova, L. & Tremaine, S. 2020, *AJ*, 160, 160
- Murray, C. D. & Correia, A. C. M. 2010, *Keplerian Orbits and Dynamics of Exoplanets*, ed. S. Seager, 15–23
- Nakamoto, T. & Nakagawa, Y. 1994, *ApJ*, 421, 640
- Oliphant, T. E. 2006, *A guide to NumPy*, Vol. 1 (Trelgol Publishing USA)
- Paardekooper, S. J., Baruteau, C., & Kley, W. 2011, 410, 293
- pandas development team. 2020, pandas-dev/pandas: Pandas
- Pecaut, M. J. & Mamajek, E. E. 2013, *ApJS*, 208, 9
- Petigura, E. A., Howard, A. W., Marcy, G. W., et al. 2017, *AJ*, 154, 107
- Pollack, J. B., Hubickyj, O., Bodenheimer, P., et al. 1996, *Icarus*, 124, 62
- Rauer, H., Catala, C., Aerts, C., et al. 2014, *Experimental Astronomy*, 38, 249
- Ricker, G. R., Winn, J. N., Vanderspek, R., et al. 2014, *Journal of Astronomical Telescopes, Instruments, and Systems*, 1, 014003
- Sandford, E., Kipping, D., & Collins, M. 2019, *MNRAS*, 489, 3162
- Santerne, A., Malavolta, L., Kosiarek, M. R., et al. 2019, 1
- Santos, N. C., Israelian, G., Mayor, M., et al. 2005, *A&A*, 437, 1127
- Sarkis, P., Mordasini, C., Henning, T., Marleau, G. D., & Mollière, P. 2021, *A&A*, 645, A79
- Schneider, J., Dedieu, C., Le Sidaner, P., Savalle, R., & Zolotukhin, I. 2011, *A&A*, 532
- Shakura, N. I. & Sunyaev, R. A. 1973, *A&A*, 24, 337
- Sing, D. K., Fortney, J. J., Nikolov, N., et al. 2016, *Nature*, 529, 59
- Thiabaud, A., Marboeuf, U., Alibert, Y., et al. 2014, *A&A*, 562 [1312.3085]
- Thompson, S. E., Coughlin, J. L., Hoffman, K., et al. 2018, *ApJS*, 235, 38
- Twicken, J. D., Catanzarite, J. H., Clarke, B. D., et al. 2018, *PASP*, 130, 064502
- Twicken, J. D., Jenkins, J. M., Seader, S. E., et al. 2016, *AJ*, 152, 158
- Tychoniec, Ł., Tobin, J. J., Karska, A., et al. 2018, *ApJS*, 238, 19
- Udry, S. & Santos, N. C. 2007, *ARA&A*, 45, 397
- Van Rossum, G. & Drake, F. L. 2009, *Python 3 Reference Manual* (Scotts Valley, CA: CreateSpace)
- Venturini, J., Guilera, O. M., Haldemann, J., Ronco, M. P., & Mordasini, C. 2020, *A&A*, 643, L1
- Venuti, L., Bouvier, J., Cody, A. M., et al. 2017, *A&A*, 599, 1
- Veras, D. & Armitage, P. J. 2004, 347, 613
- Virtanen, P., Gommers, R., Oliphant, T. E., et al. 2020, *Nature Methods*
- Wang, S. 2017, *Research Notes of the American Astronomical Society*, 1, 26
- Waskom, M. & the seaborn development team. 2020, mwaskom/seaborn
- Weiss, L. M., Marcy, G. W., Petigura, E. A., et al. 2018, *AJ*, 155, 48
- Weiss, L. M. & Petigura, E. A. 2020, *ApJ*, 893, L1
- Williams, J. P. & Cieza, L. A. 2011, *ARA&A*, 49, 67
- Winn, J. N. 2010, arXiv e-prints, arXiv:1001.2010
- Winn, J. N. & Fabrycky, D. C. 2015, *ARA&A*, 53, 409
- Winn, J. N., Sanchis-Ojeda, R., & Rappaport, S. 2018, *New A Rev.*, 83, 37
- Xu, W., Lai, D., & Morbidelli, A. 2018, 481, 1538
- Youdin, A. 2008, in *EAS Publications Series*, ed. T. Montmerle, D. Ehrenreich, & A. M. Lagrange (EAS Publications Series)
- Zar, J. H. 2014, *Biostatistical Analysis*, 5th edn. (Essex: Pearson), 761
- Zhu, W. 2020, *AJ*, 159, 188

Appendix A: Detection biases explain the negative correlation between mutual separation and average sizes/masses

In their effort to study the connection between planetary sizes and their orbital spacing, W18 explored the mutual separation (in units of mutual hill radii) between planets. The mutual separation between two adjacent planets is defined using their mutual hill radius R_H^{mutual} . The mutual hill radius of two adjacent planets (with masses m_j and m_{j+1}) can be thought of as the hill sphere radius of a single planet located between the two adjacent planets and whose mass is the sum of the two planets. This gives,

$$R_H^{\text{mutual}} = \left(\frac{m_j + m_{j+1}}{3 M_\star} \right)^{1/3} \left(\frac{a_j + a_{j+1}}{2} \right) \quad (\text{A.1})$$

Here, M_\star is the stellar mass while a_j and a_{j+1} are the star-planet distances. The mutual separation, Δ , between two planets is the ratio of their orbital separation to their mutual hill radius. It measures the dynamical spacing between two planets in units of their mutual hill radius.

$$\Delta = \frac{a_{j+1} - a_j}{R_H^{\text{mutual}}} \quad (\text{A.2})$$

W18 find that there is a significant negative correlation between mutual separation and the average size of adjacent planets in the CKSM catalogue ($R = -0.2$). They state: “The mutual Hill radius incorporates the mass of the planet, and so ideally, the computation of mutual Hill radius separation should remove the contribution of planet size.” Further, they add: “This correlation is driven by an absence of points in the lower left corner of the plot. (...) and so the absence of very small planets at close dynamical spacings is not due to detection bias.”

Here, the same connection is explored through the 100 embryo theoretically observed KOBE and the theoretical underlying Bern Model population. In Fig. A.1 (top left) the average radius of two adjacent planets (in KOBE) is plotted as a function of their mutual hill separation. The period ratio of the adjacent planets is marked in colour. In good agreement with W18, there is a significant negative correlation which is confirmed by a Pearson correlation test ($R = -0.1$).

To test whether this correlation arises from detection biases, the same correlation test was also done for the theoretical underlying population. Figure A.1 (bottom left) shows the average radius as a function of mutual Hill separation for two adjacent planets. The correlation test finds a significant positive correlation. Interestingly, the lower left corner of the plot, which was empty for the KOBE population, is filled for the underlying population. Since the negative correlation only exists in the theoretically observed KOBE population but not in the underlying NGPPS population, this clearly demonstrates that the negative correlation found in the KOBE population is due to detection biases. This suggests that the negative correlation seen in CKSM is, probably, also due to detection biases.

One of the findings of this paper is that the size trends are derivative of the mass trends. To test this further, the average mass of adjacent planets is plotted as a function of their mutual Hill radii in Fig. A.1 (right). The top plot is for the theoretically observed planetary populations (KOBE) and the bottom plot is for the theoretical underlying population. The KOBE population shows a significant negative correlation with $R = -0.08$, while the underlying population shows a stronger positive correlation. This behaviour is similar to the correlations between

average sizes and mutual separation, as seen before. In the plot with average masses, adjacent planets of constant period ratios lie on straight lines (i.e. points of same colour). In the plot with average sizes, adjacent planets of constant period ratios tend to be on straight lines, but show considerable scatter for average sizes $> 3 R_\oplus$. This scatter can be traced to the intrinsic scatter in the radius of planets with size $> 3 R_\oplus$ in the mass-radius diagram in Fig. 8.

The negative correlation in the average mass versus mutual Hill plot comes from the $\frac{1}{3}$ power on the mass term in eq. A.1. It gives average masses a slope of -3 on the logarithmic average mass vs mutual Hill plane. To visualize this, the $y \propto x^{-3}$ dependence is plotted as a dashed line in Fig. A.1 (right). The slope of this line matches very well with the underlying points. This demonstrates that the negative correlation seen in the KOBE plots (top row) is due to the definition of mutual separation itself.

There is, nevertheless, an important role played by detection biases. Why does the theoretically observed population (KOBE) show no adjacent pairs with small sizes/mass and low mutual separation? This is understandable due to the detection biases of the transit method.

The Hill sphere radius of a planet defines the region around a planet, in which the gravitation field of the planet dominates. As the star-planet distance increases, the influence of the star diminishes and R_H of a planet increases. This can be seen through eq. B.5. This is also true for the mutual Hill radii, R_H^{mutual} . As two adjacent planets move further out, their mutual Hill radii increases. The inverse dependence of Δ on R_H^{mutual} implies that as the mutual Hill separation between adjacent planets increases, their mutual separation decreases. Consider two planets with fixed orbital separation, $a_{j+1} - a_j$. When these two planets are close to the host star, their mutual Hill radius is small resulting in large mutual separation (in Hill units) between them. However, if the same two planets are located further away from the host star, their mutual Hill radius increases, which in turn causes their mutual separation Δ to decrease. The planets now have lower dynamical spacing owing to the weakening gravitation effect from the host star. Thus, as two planets, with constant orbital separation, move away from their star their mutual separation decreases.

Since detection biases of the transit method disfavour the discovery of small planets further out from their host star, this explains why planets with small average sizes/mass are missing from the lower left corner in the KOBE plots (top row). Detection biases, indeed, explain the absence of small planets at close dynamical spacing.

Appendix B: The Bern Model – Additional details

Appendix B.1: Before planet formation begins

Appendix B.1.1: Stellar Evolution

The model includes the evolution of a fixed mass star ($M_\star = 1 M_\odot$) by incorporating the stellar evolution tracks from Baraffe et al. (2015). The evolving stellar properties influence the behaviour of the disk and the growing planets in multiple ways. For example, stellar irradiation and temperature (L_\star, T_\star) affects the thermodynamical aspects of both the disks and the planets. Stellar radius R_\star strongly affects the transit signal generated by a transiting planet and also allows the tracking of collisions between any object and the star.

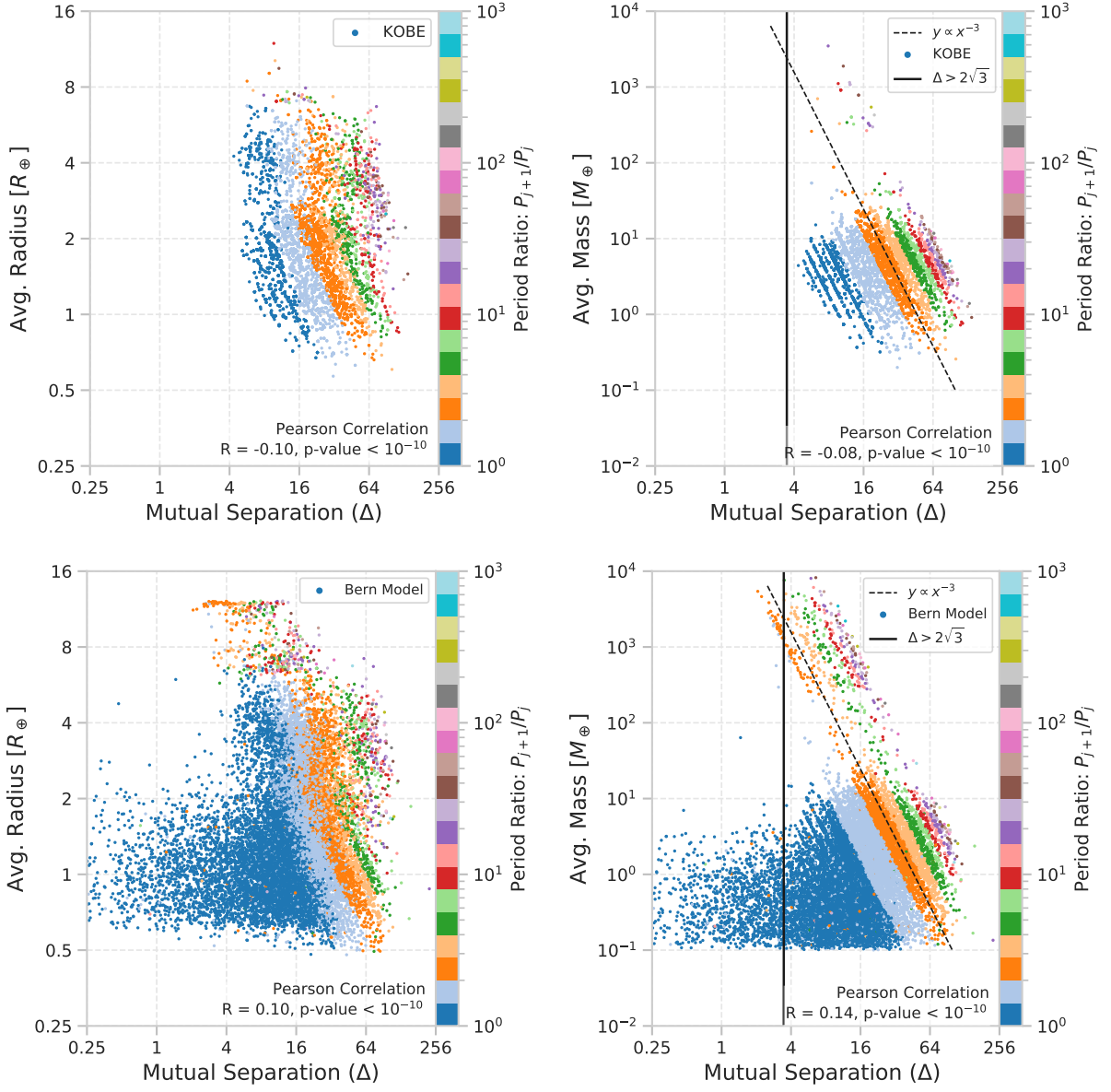


Fig. A.1. The dependence of mutual separation of adjacent planets on their average sizes (left) and average masses (right). The top row corresponds to the theoretically observed KOBE population, while the bottom row shows the same for the theoretical underlying 100 embryo population. Observed exoplanetary populations (CKSM by W18) show a negative correlation between average sizes and mutual separation of adjacent planets which is well reproduced here (top left). However, this negative correlation arises from the dependence of mutual Hill radii on the $1/3^{rd}$ power of planetary masses. This is shown by the dashed line in the plots on the right. The underlying population fills the lower left corner of the plot, which is empty in the top row. Detection biases explain the lack of small sized planets with low dynamical spacing. The vertical line marks the Hill stability criterion from Chambers et al. (1996). Points on the right side of this line are Hill stable ($\Delta > 2\sqrt{3}$).

Appendix B.1.2: Protoplanetary Disk - Gaseous phase

The gas disk plays a crucial role in the growth of planets and shaping the planetary system architectures. Accretion of this nebular gas may lead to gaseous envelopes around many planets. Additionally, the gas disk interacts with planetesimals, embryos and protoplanets through effects such as gas drag, migration, and eccentricity damping.

The model follows the evolution of an axisymmetric, geometrically thin gas disk in a time-independent gravitational potential. Gas is accreted by the star and growing planets, and is lost via photoevaporation. Meanwhile, the outer regions of the disk are pushed away to conserve angular momentum until the disk is completely dissipated. The disk evolution is computed

in the region from r_{in} up to $r_{\text{max}} = 1000$ au. Here, r is the radial distance from the star and r_{in} is a Monte-Carlo variable for the model (discussed in Sect. 3). The vertically-integrated and azimuthally-averaged surface density of gas Σ_g , evolves as,

$$\dot{\Sigma}_g(r) = \frac{1}{r} \frac{\partial}{\partial r} F(r) - \dot{\Sigma}_{g,\text{photo}}(r) - \dot{\Sigma}_{g,\text{planet}}(r), \quad (\text{B.1})$$

where F is radial flux of gases from viscous angular momentum transport (Lüst 1952; Lynden-Bell & Pringle 1974) $F(r) = 3r^{1/2} \frac{\partial}{\partial r} (r^{1/2} \Sigma_g \nu)$. Effective turbulent viscosity, ν , is parametrized by a dimensionless parameter α as $\nu = \alpha c_s h$ (following Shakura

& Sunyaev 1973)¹⁹. Here, c_s is the isothermal speed of sound (depends on temperature and mean molecular mass of gas), and h is the local disk pressure scale height (\sim half of disk thickness). Following observations (Manara et al. 2019; Flaherty et al. 2020), in this work $\alpha = 2 \times 10^{-3}$.

The Extreme UV and Far UV radiations from the host star and neighbouring stars, respectively, heat the disk such that thermal motion can overcome gravitational potential resulting in the dispersal of the disk (Clarke et al. 2001; Matsuyama et al. 2003). Following Mordasini et al. (2012b), internal and external photoevaporation losses are included in $\dot{\Sigma}_{g,photo}$. These mechanisms control disk lifetime via the mass loss rate, \dot{M}_{wind} , which is a Monte-Carlo variable for the model and is discussed in Sect. 3. The disk also loses some amount of gas to planetary accretion, which is represented by $\dot{\Sigma}_{g,planet}$ ²⁰.

The model begins with an initial surface density profile for the gas disk given by (Veras & Armitage 2004),

$$\Sigma_g(r) = \Sigma_{g,0} \left(\frac{r}{5.2 \text{ au}} \right)^{-\beta_g} \exp \left(\left(\frac{r}{r_{cut,g}} \right)^{\beta_g - 2} \right) \left(1 - \sqrt{\frac{r_{in}}{r}} \right),$$

$$\beta_g = 0.9 \text{ (Power Law Index).} \quad (\text{B.2})$$

Here, $\Sigma_{g,0}$ (normalization constant) and $r_{cut,g}$ (characteristic radius) are governed by a Monte-Carlo variable, M_g , the initial gas disk mass through the relations (see Paper II),

$$M_g = \Sigma_{g,0} \left[\left(\frac{2\pi}{2 - \beta_g} \right) \left(\frac{1}{5.2 \text{ au}} \right)^{-\beta_g} \left(\frac{1}{r_{cut,g}} \right)^{2 - \beta_g} \right],$$

$$M_g = 2 \times 10^{-3} M_\odot \left(\frac{r_{cut,g}}{10 \text{ au}} \right)^{1.6}. \quad (\text{B.3})$$

The flaring disk gains thermal energy from the host star, viscous dissipation and a background thermal radiation (at 10 K). For thermal equilibrium, the disk cools down by radiating away this energy from its surface (Alibert et al. 2005; Fortier et al. 2013). Assuming the disk is in hydrostatic equilibrium, the local energy produced due to viscosity is removed through radiative flux, which has to diffuse towards the disk-surface²¹. Considering radiative transfer through optically thick and thin regions allows the evaluation of the mid-plane disk temperature (following Nakamoto & Nakagawa 1994; Hueso & Guillot 2005). The disk temperature impacts planetary interiors and their growth rates.

Appendix B.1.3: Protoplanetary Disk - Planetesimals

Planetary embryos, initially, grow by accreting planetesimals from the solid disk to become planetary cores. The planetesimal disk is modelled as a fluid with surface density Σ_s (Fortier et al. 2013). This disk evolves via planetary accretion, aerodynamic interaction with nebular gas and viscous stirring from planets or planetesimals. The interactions excite planetesimal eccentricity and inclination, possibly resulting in ejection of some solids, which influences the rate at which they are accreted by embryos. For simplicity, two kinds of planetesimals are assumed: rocky (refractory materials) with $\rho_{plan} = 3.2 \text{ g cm}^{-3}$ and icy (volatile

rich) with $\rho_{plan} = 1.0 \text{ g cm}^{-3}$ of equal and fixed size of 300 m. The initial surface density profile is (see Paper II for details),

$$\Sigma_s(r) = \Sigma_{s,0} \left[f_s(r) \left(\frac{r}{5.2 \text{ au}} \right)^{-\beta_s} \exp \left(- \left(\frac{r}{r_{cut,s}} \right)^{\beta_s - 2} \right) \right],$$

$$\beta_s = 1.5 \text{ (Power Law Index),}$$

$$r_{cut,s} = \frac{r_{cut,g}}{2}. \quad (\text{B.4})$$

Here, $\Sigma_{s,0}$ allows the mass of solid disk to be fixed as $M_s = M_g f_{D/G}$. The dust to gas ratio, $f_{D/G}$, is a Monte-Carlo variable (see Sect. 3). The rocky-to-ice ratio $f_s(r)$ is the ratio of condensed solid to total solids (following Thiabaud et al. 2014).

Appendix B.2: Planet Formation

Appendix B.2.1: Accretion of Solids

Protoplanetary embryos accrete planetesimals from their feeding zone, which is defined as an annulus on each side of the embryos' orbit. The width of the feeding zone is given in terms of the hill radius R_H :

$$r_{feed} = \mu R_H, \quad (\mu = 5, \text{ Fortier et al. (2013)})$$

where,

$$R_H = a_M \left(\frac{M_{planet}}{3M_\star} \right)^{1/3}. \quad (\text{B.5})$$

Competition for solids occurs when the feeding zone of multiple planets overlap (Alibert et al. 2013). The overlapping feeding zone, with surface density $\bar{\Sigma}_s$, is separated into individual regions for each planet (see Paper I). The accretion rate (\dot{M}_{core}) of planetesimals of spherical radius R_{plan} by an embryo of core mass M_{core} depends on the probability of a protoplanet-planetesimal collision p_{coll} , angular velocity Ω (which is $\sqrt{GM_\star/r^3}$), $\bar{\Sigma}_s$, and R_H .

$$\dot{M}_{core} = \Omega \bar{\Sigma}_s R_H^2 p_{coll}(R_{plan}, R_H, r_{capture}, v_{rel}) \quad (\text{B.6})$$

The collision rates, in turn, depend on the dynamical evolution of the solid disk. Planetesimals experience aerodynamic drag forces from the gas, and interact gravitationally with the protoplanets and amongst themselves. These interactions influence the relative velocity, v_{rel} , between the two colliding bodies. Additionally, when planets become massive ($\gtrsim 1 M_\oplus$) their gas envelope affects the dynamics of penetrating solids. This results in an enhancement of the planetesimal capture radius $r_{capture}$.

Appendix B.2.2: Accretion of Gases

The accretion of gas by a planet depends on the local thermodynamical state of the protoplanetary disk and, interestingly, on the planetary interior as well. The internal structure of the planet is obtained by demanding conservation of mass, hydrodynamic equilibrium and that energy diffusion be either radiative or convective. The demand for energy conservation is implemented through an iterative scheme which searches for a solution that is consistent with the boundary conditions (see Paper I; Mordasini et al. (2012c)).

Initially, the gaseous envelope around all planets transitions smoothly into the nebular gas, the so called *attached* phase (see panel (d) in Fig. 1). In attached phase, gas from the nebular disk flows into the planet to compensate for planetary contraction.

¹⁹ α measures efficiency of transport due to turbulence. Since, random isotropic motions do not have length-scales larger than the local disk scale height, α is usually < 1 (King 2009).

²⁰ In the first $\sim 10^5$ year, the disk gains mass from the molecular cloud collapse. This can be modelled by adding a source term to eq. B.1 as is done in Hueso & Guillot (2005).

²¹ This is because: (a) the disk is geometrically thin and (b) the disk is assumed to be optically thick along the radial direction.

Planets contract as they cool down by radiating away the energy gained through accretion. The surface pressure and temperature of the planet are balanced with those of disk mid plane. When a planet reaches a critical threshold mass, large radiative losses cannot be balanced by accretional energy and further contraction of the envelope ensues. This results in even larger gas accretion, further increasing the accretional energy – runaway accretion of gas is inevitable. Consequentially, planets gain a massive envelope very rapidly becoming giant planets.

For planetary cores massive enough to undergo runaway gas accretion, the rate of gas accretion may exceed the ability of the disk to supply gas (the maximum gas accretion rate). Then, the envelope detaches from the gas disk and the planet continues to accrete in this *detached* phase. In detached phase, gas accretion does not depend on the planetary internal structure, but on the protoplanetary gas disk. The planet’s radius contracts very rapidly to $\sim R_J$, as it adjusts to new boundary conditions.

The last phase of planetary evolution, common to all planets, is the *isolated* phase, which occurs after the gas disk has dissipated. Gas accretion comes to a halt and planets will now contract as they cool down.

Appendix C: KOBE – Additional details

Appendix C.1: KOBE-Shadows

Whether a planet can transit for a given observer, is determined by KOBE-Shadows. For this, the *transit shadow band* (TSB) is determined by examining transit geometry, as shown in Fig. C.1 (left). A planet orbiting a star will intercept some of the starlight, casting its shadow on a celestial sphere centred on this star. As the planet moves in its orbit the planet’s shadow traces a shadow band on the celestial sphere. The area on the celestial sphere which falls inside a planet’s shadow constitutes the TSB.

All observers inside a planet’s TSB can potentially detect this planet via its transit. This planet will not appear to be transiting to any observer who is outside the planet’s TSB. KOBE-Shadows utilizes this distinction between transiting and non-transiting planets to detect the former.

To compare with Kepler, simulating $\sim 200\,000$ stars in NGPPS is computationally expensive. KOBE-Shadows offers a convenient solution. Using transits, a single observer may never find all the planets in a planetary system. This could occur either when TSB from all planets never overlap or when the location of an observer is outside the TSB of some planets. These are the basic geometrical limitations of the transit method. When the same system is observed by another observer located elsewhere, they may find different transiting planets than those found by the first observer. This means that two observers can view two different subsets of the same planetary system. By analysing the transit geometry of a planetary system for several observers, KOBE-Shadows generates multiple subsets of transiting systems (one from each observer). Subsequent modules in KOBE treat these subsystems, KOBE systems, as independent planetary systems. This allows KOBE to emulate observations of 200 000 stars from 1 000 NGPPS systems. Additional steps are taken in other modules to ensure that these system are treated independently²². KOBE systems with at least one transiting planet

form the KOBE-Shadows catalogue, which is analysed in subsequent modules.

To compute the TSB for multiple planets in a system, KOBE-Shadows requires:

- Stellar and planetary radii, $(R_\star, R_{\text{planet}})$: These are provided by the Bern Model and they evolve with time.
- Orbital elements $(a, e, i, \Omega, \omega, \bar{f})$: The six orbital elements are semi-major axis a , eccentricity e , inclination i , longitude of ascending node Ω , argument of periape ω , and true anomaly \bar{f} . The first two elements describe the 2D shape of an elliptical orbit. The next three orbital elements define the relative orientation of an orbit in 3D space. The last element gives the position of a planet on its orbit with respect to the periastron²³. The Bern Model provides all of these elements for all planets. However, an orbit’s inclination as calculated in the model is with reference to the original protoplanetary disk, as opposed to any observer’s reference sky-plane. These values are calculated only during the N -body stage. A planet’s period P is calculated as: $P^2 = \frac{4\pi^2}{GM_\star} a^3$.
- Location of Observer, $O_i(\theta, \phi)$: The location of an observer is specified in a standard coordinate system (X, Y, Z) . The origin is at the star (see Fig. C.1 (left)). X -axis is along a reference line and (X, Y) define a reference plane (Z is perpendicular to this plane). An observer’s location is specified in polar co-ordinates by an azimuth angle $\theta \in [0, 2\pi]$ and a polar angle $\phi \in [0, \pi]$. The subscript i is used to distinguish between multiple observers, and two observers are not allowed to be at the same location. Bern Model does not provide the location of any special observer. It is assumed that the location of observers does not evolve with time.

The calculation procedure implemented in KOBE-Shadows is as follows:

1. Number of observers, n_{obs} : It is fixed by the number of stars observed by a survey, $n_{\star, \text{survey}}$ and the number of synthetic systems (at time t) in a population, $n_{\text{system}}(t)$. The relation is

$$n_{\text{obs}} = \frac{n_{\star, \text{survey}}}{n_{\text{system}}(t)}. \quad (\text{C.1})$$

Fixing $n_{\star, \text{survey}}$ to 200 000 for Kepler, a population with $n_{\text{system}}(t) = 1\,000$ would require 200 observers. Although all three populations simulate 1 000 systems, $n_{\text{system}}(t)$ may diminish with time. For the nominal populations, at 4 Gyr, NG74 has 998, NG75 has 999 and NG76 has 1 000 systems.

2. Location of observers: The observers are distributed uniformly and homogeneously around the celestial sphere, in the (X, Y, Z) coordinate system. This is done by generating two different random numbers $u_1, u_2 \in [0, 1]$ and using inverse transform sampling to obtain polar coordinates, as:

$$\theta = 2\pi u_1, \quad \text{and} \quad \phi = \cos^{-1}(1 - 2u_2). \quad (\text{C.2})$$

This initial location of observers remains fixed for one NGPPS system. Spherical coordinates are converted to

effect of transit probability (via TSB calculation), and (c) systematize KOBE’s approach.

²³ A planet’s position on the orbit, \bar{f} , is not required to calculate its TSB. This is because the calculation is done for virtually all positions on the orbit.

²² It is emphasized that KOBE systems, being subsets of the NGPPS systems, are not truly independent. In KOBE, a single observer observing 1 000 synthetic planetary systems may detect ~ 100 transiting planets around ~ 50 stars. The strategy of using multiple observers in KOBE grew out of a need to (a) find more transiting planets, (b) imprint the

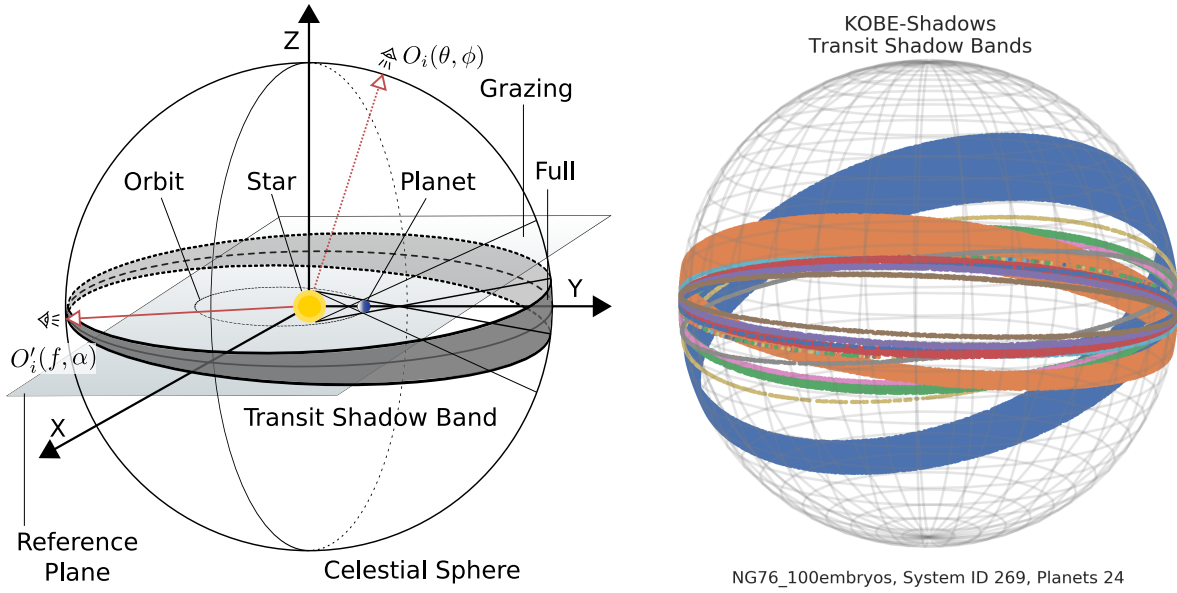


Fig. C.1. Left: Transit geometry for a single star-planet system. The dashed red arrow represents the initial location of an observer $O_i(\theta, \phi)$, and the solid red arrow marks the rotated location of same observer $O'_i(f, \alpha)$ (see text for details). Right: An example of transit shadow bands for a 24 planet system (star/planets are not shown). KOBE-Shadows calculates whether an observer is present inside the full transit shadow band of any planet in this system. The innermost planet has $P_{\text{tra}} = 12\%$ and is detectable by observers marked in blue. The second ($P_{\text{tra}} = 6\%$) and the third innermost planet ($P_{\text{tra}} = 2\%$) are detectable by observers marked in orange and green respectively. The probability to potentially detect any 4 planets simultaneously via transit for this system is $\sim 8\%$, which is halved for simultaneously detecting any 9 planets.

Cartesian giving $\mathbf{v}_{(X,Y,Z)}$, the unit-normed vectorial location of an observer.

- Aligning transit geometry: Bern Model gives the position of a planet and its orbit in a different coordinate system, (x, y, z) with origin at the star. Here, x is along the periastron, (x, y) are in the orbital plane and z points along the angular momentum vector of the planet. To proceed, the two coordinate systems must be aligned. This is done by rotating the initial location of all observers (given in (X, Y, Z) coordinates) with respect to each planet's orbit (given in (x, y, z) coordinates) via three rotations (for details see Murray & Correia (2010))²⁴:

$$\mathbf{v}'_{(x,y,z)} = R_Z^{-1}(\omega) R_X^{-1}(i) R_Z^{-1}(\Omega) \mathbf{v}_{(X,Y,Z)}. \quad (\text{C.3})$$

Here, $R_X^{-1}, R_Y^{-1}, R_Z^{-1}$ are the inverses of the standard SO(3) rotation matrices. $R_Z^{-1}(\Omega)$ aligns the line of nodes with X -axis. $R_X^{-1}(i)$ aligns the reference plane with the orbital plane. $R_Z^{-1}(\omega)$ rotates the reference plane such that the X -axis points along the periastron point of the orbit. The new location of the observer is given by the vector $\mathbf{v}'_{(x,y,z)}$ and in polar coordinates $O'_i(f, \alpha)$. In Fig. C.1 (left), an example of such rotation is shown.

Now the location of observers and the planetary orbits is known in the same coordinate system. This step ensures relative orientation between different planets is maintained and information coming from all orbital elements is used.

- Angular Width of TSB: The semi cone angle ψ , subtended by the planet's shadow as it blocks starlight, at azimuthal

location of observer $O'_i(f, \alpha)$ is given by (Winn 2010),

$$\sin(\psi) = \left(\frac{R_\star \pm R_{\text{planet}}}{r_{\text{planet}}} \right), \quad \begin{cases} + & \text{include grazing transits} \\ - & \text{exclude grazing transits} \end{cases}$$

$$r_{\text{planet}} = \frac{a(1 - e^2)}{1 + e \cos(f)}. \quad (\text{C.4})$$

Here, r_{planet} is the star-planet distance when the planet's true anomaly is $\bar{f} = f$ ²⁵. Finally, it is checked whether the observer $O'_i(f, \alpha)$ is inside the TSB through the following condition:

$$\alpha \in \left[\frac{\pi}{2} - \psi, \frac{\pi}{2} + \psi \right] \rightarrow \text{Inside TSB},$$

$$\text{otherwise} \rightarrow \text{Outside TSB}. \quad (\text{C.5})$$

This information is now stored for a planet at the original location of the observer $O_i(\theta, \phi)$.

- Repeat from step 4, for all n_{obs} observers.
- Repeat from step 3, for all planets in a system.
- Repeat from step 2, for all systems in a population.

Figure C.1 (right) displays the result from KOBE-Shadows for a system with 24 planets in NG76. This calculation, done using 10^6 observers and considering only full transits, takes about 1s.

These calculations undergo two major consistency checks. First, the area under a planet's TSB over the area of the celestial sphere gives the transit probability for this planet. Here, the number of observers found inside a TSB over n_{obs} gives a numerical proxy for the same. The analytical expression for transit

²⁴ Equivalently, one could rotate a planet's orbit, keeping the location of observers fixed.

²⁵ For this paper, grazing transits are excluded.

probability, P_{tra} , of a planet can be easily derived, [Barnes \(2007\)](#):

$$P_{\text{tra}} = \frac{R_{\star} \pm R_{\text{planet}}}{a(1 - e^2)}, \quad \begin{cases} + & \text{include grazing transits} \\ - & \text{exclude grazing transits} \end{cases} \quad (\text{C.6})$$

The numerical and analytical values of P_{tra} , with varying n_{obs} from 10^5 to 10^8 , are found to be in good agreement. In addition, the transit probability for multiple planets is available for free via the numerical recipe described above. Finding the same through analytical approaches is a difficult problem.

Secondly, the impact parameter of a transiting planet for all observers inside TSB should be less than $1 + (R_{\text{planet}}/R_{\star})$. The impact parameter, b , is the sky-projected star-planet distance expressed in units of stellar radii, and is given by:

$$b = \frac{r_{\text{planet}}}{R_{\star}} \cos(i). \quad (\text{C.7})$$

The impact parameter for an observer $O_i(f, \alpha)$, is calculated by identifying $i = \alpha$. This condition is satisfied by all observers that are inside the TSB, for all planets, for all systems, in all three populations.

The above procedure produces the KOBE-Shadows catalogue which consists of KOBE Systems containing (at least one) transiting planets. Although, all of the planets in this catalogue will transit, but not all of them will be detected. KOBE-Transits takes care of this problem.

Appendix C.2: KOBE-Transits

KOBE-Transits examines the transit signal for all transiting planets found by KOBE-Shadows. To be detected, a transiting planet has to produce a signal which is strong enough to be detected by observers. To check this, KOBE-Transits calculates the transit SNR. For this, an estimate of the noise as seen by an observer is required.

In KOBE-Transits, noise for a KOBE System is sampled from the distribution of rms combined differential photometric precision (CDPP). Produced by the Kepler pipeline (DR25) for individual target stars, CDPP is an empirical measure of the stellar photometric noise ([Christiansen et al. 2012](#))²⁶. Three cuts are placed on this distribution to ensure that FGK-Solar type stars are sampled. These are on mass $M_{\star} \in [0.7, 1.3]M_{\odot}$, radius $R_{\star} \leq 5 R_{\odot}$, and on stellar temperature $T_{\star} \in [3880, 7200]\text{K}$ ([Pecaut & Mamajek 2013](#)).

The amount of stellar flux blocked by a planet is proportional to its area. The transit signal generated by a single transit is $\delta = (R_{\text{planet}}^2/R_{\star}^2)$. The single transit SNR is,

$$\text{SNR} = \frac{\delta}{\text{CDPP}_{\text{eff}}}, \quad \text{single transit}$$

$$\text{CDPP}_{\text{eff}} = \text{CDPP}_{t_{\text{trial}}} \left(\frac{t_{\text{trial}}}{t_{\text{dur}}} \right)^{\frac{1}{2}}. \quad (\text{C.8})$$

Here, CDPP_{eff} is the effective stellar noise seen by an observer during a transit of duration t_{dur} . $\text{CDPP}_{t_{\text{trial}}}$ is the rms CDPP calculated by Kepler pipeline for different trials of transit durations (varying from 1.5 h to 15 h). Following [W18](#), here $t_{\text{trial}} = 6\text{h}$. Figure C.2 (left) shows the distribution of rms $\text{CDPP}_{6\text{h}}$ after placing the above cuts. To enhance the independent treatment

of KOBE Systems, a noise value is drawn randomly from the rms $\text{CDPP}_{6\text{h}}$ distribution for every star in the KOBE-Shadows catalogue.

Transit duration for a planet is estimated by the time taken by a planet to cross the stellar disk. Following [W18](#), circular orbits and $b = 0$ are assumed. This gives,

$$t_{\text{dur}} = \frac{2R_{\star}}{\left(\frac{2\pi a}{P}\right)} = \frac{R_{\star}P}{\pi a}. \quad (\text{C.9})$$

When a planet's transit is observed n_{tra} times, the multi-transit SNR improves by a factor of $\sqrt{n_{\text{tra}}}$. For a planet with period P and transit survey of duration t_{survey} , the average number of transits can be estimated as $n_{\text{tra}} = t_{\text{survey}}/P$. Then, the multi-transit SNR generated by a transiting planet for $t_{\text{survey}} = t_{\text{kepler}} = 3.5\text{ yr}$ is,

$$\text{SNR} = \underbrace{\left(\frac{R_{\text{planet}}}{R_{\star}}\right)^2}_{=\delta} \underbrace{\left(\frac{R_{\star}}{a}\right)^{\frac{1}{2}}}_{=P_{\text{tra}}} \left[\left(\frac{t_{\text{kepler}}}{\pi t_{\text{trial}}}\right)^{\frac{1}{2}} \frac{1}{\text{CDPP}_{t_{\text{trial}}}} \right]. \quad (\text{C.10})$$

This formulation shows that the transit SNR is given by the transit signal generated by a planet, weighed by the probability of its transit (assuming circular orbits), scaled with instrument and survey related constants. Thus, a large planet, closely-orbiting a small quiet star will produce a large SNR. These are some of the detection biases of the transit method.

In KOBE-Transits, transiting planets that have $\text{SNR} \geq 7.1$ and $n_{\text{tra}} \geq 2$ constitute the KOBE-periodic threshold crossing event (pTCE) catalogue. For Kepler pipeline, the threshold for detection of a TCE was multiple-event statistic (MES, analogous to multi-transit SNR) $\geq 7.1\sigma$, and $n_{\text{tra}} \geq 3$ ([Twicken et al. 2016, 2018](#); [Christiansen et al. 2012](#); [Thompson et al. 2018](#)). Following [W18](#), minimum n_{tra} is fixed to 2.

Appendix C.3: KOBE-Vetter

In [Thompson et al. \(2018\)](#), the DR25 TCE are further reviewed by an automatic program, the Robovetter. The Robovetter examines several metrics and dispositions consistent TCEs as Kepler Object of Interest (KOIs). Through further analysis, the Robovetter eventually vets KOIs as either planet candidates or false positive. However, not all candidates are true exoplanets and some false positives may have been genuine signals.

The catalogue produced by the Robovetter was characterized for completeness and reliability. Completeness measures the fraction of true planets that are absent in the catalogue, and reliability measures the fraction of planetary candidates that are truly exoplanets ([Coughlin 2017](#)). These measurements are done by injecting simulated transit signal in the Robovetter. The Robovetter completeness is given by the fraction of injected transit signal that are dispositioned as planetary candidates. The confidence of vetting a TCE as planetary candidates is expressed with a disposition score (ranging 0 to 1, higher value implying higher confidence that a TCE is a candidate). Selecting only high scoring candidates produces a catalogue which has less completeness, but is highly reliable.²⁷

KOBE-Vetter calculates the Robovetter completeness (for disposition score ≥ 0.9) using the results of these injection tests

²⁷ [Thompson et al. \(2018\)](#) suggested using a cut on disposition score for occurrence rate studies. This approach has been used by [Mulders et al. \(2018\)](#) and [Hsu et al. \(2018\)](#), and extensively studied by [Bryson et al. \(2020\)](#).

²⁶ This data is available in tabular format from the [NASA Exoplanet Archive](#).

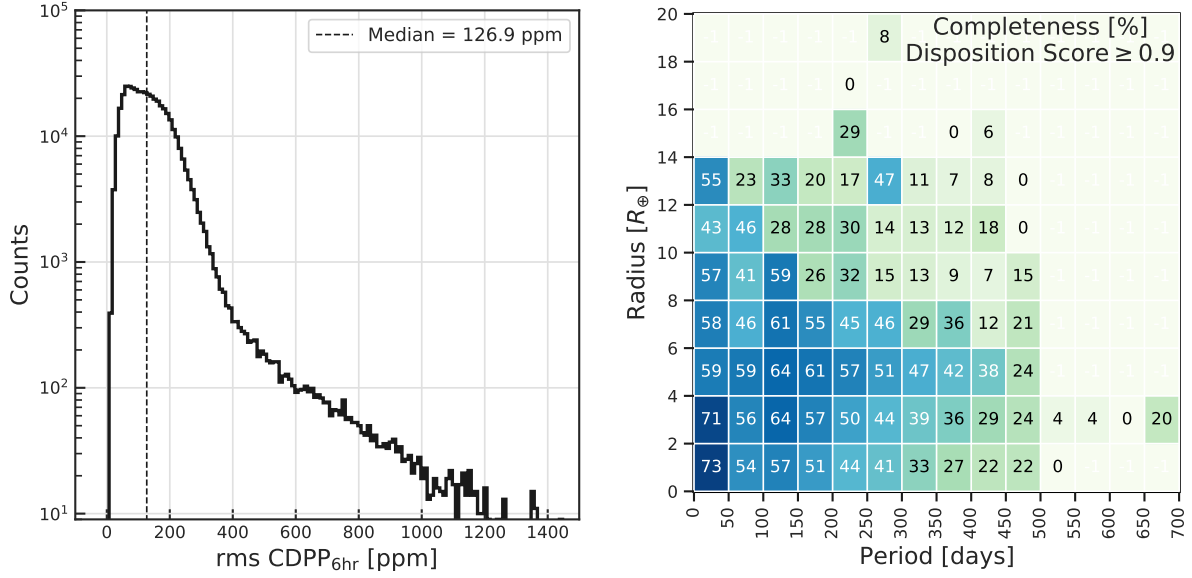


Fig. C.2. Left: Distribution of stellar noise, rms CDPP_{6h}, as seen by Kepler for FGK Solar-type stars. Each individual KOBE System is assigned a CDPP value from this distribution. Right: A 2D histogram depicting completeness of Kepler’s Robovetter as calculated by KOBE-Vetter. To emulate high reliability, a disposition score cut off is placed. Labels on each bin indicate the completeness (in %) for that bin. This calculation is based on the injected transit signals (Coughlin 2017). Completeness is not calculated for bins with less than 10 injected signals (marked with no labels). These bins are assigned a completeness of 0%.

(Coughlin 2017)²⁸. Completeness is calculated as a function of planetary radius (bin size $2 R_{\oplus}$) and period (bin size 50 d). Figure C.2 (right) shows a 2D histogram of completeness (including reliability). These values are applied on the *p*TCE catalogue, in a straightforward manner. If a 2D-bin has completeness of $C\%$, then for all planets in the *p*TCE catalogue which fall in this bin $C\%$ are randomly vetted as candidates and make the planetary candidates catalogue. The rest are rejected as false positives. For example, if there are 100 planets with $R_{\text{planet}} \in [0, 2) R_{\oplus}$ and $P \in [300, 350)$ d in the *p*TCE catalogue, then 33 planets will be randomly marked as candidates and the remaining 66 planets are vetted as false positives.

²⁸ The Robovetter Disposition Table is available from the [NASA Exoplanet Archive](#).